# A Pressure Relaxation Closure Model for One-Dimensional, Two-Material Lagrangian Hydrodynamics Based on the Riemann Problem

James R. Kamm[1],[*] and Mikhail J. Shashkov[2]

[1] *Applied Physics Division, Los Alamos National Laboratory, Los Alamos, NM 87545, USA.*
[2] *Theoretical Division, Los Alamos National Laboratory, Los Alamos, NM 87545, USA.*

**Abstract.** Despite decades of development, Lagrangian hydrodynamics of strength-free materials presents numerous open issues, even in one dimension. We focus on the problem of closing a system of equations for a two-material cell under the assumption of a single velocity model. There are several existing models and approaches, each possessing different levels of fidelity to the underlying physics and each exhibiting unique features in the computed solutions. We consider the case in which the change in heat in the constituent materials in the mixed cell is assumed equal. An instantaneous pressure equilibration model for a mixed cell can be cast as four equations in four unknowns, comprised of the updated values of the specific internal energy and the specific volume for each of the two materials in the mixed cell. The unique contribution of our approach is a physics-inspired, geometry-based model in which the updated values of the sub-cell, relaxing-toward-equilibrium constituent pressures are related to a local Riemann problem through an optimization principle. This approach couples the modeling problem of assigning sub-cell pressures to the physics associated with the local, dynamic evolution. We package our approach in the framework of a standard predictor-corrector time integration scheme. We evaluate our model using idealized, two material problems using either ideal-gas or stiffened-gas equations of state and compare these results to those computed with the method of Tipton and with corresponding pure-material calculations.

*Corresponding author. *Email addresses:* `jrkamm@sandia.gov` (J. R. Kamm), `shashkov@lanl.gov` (M. J. Shashkov)

# 1   Introduction

Multi-material Lagrangian hydrodynamics of strength-free materials continues to present numerous open issues, even in one dimension. We focus on the problem of closing a system of equations for a two-material cell under the assumption of a single velocity model. We treat the constituents in these multi-material cells as distinct, i.e., we do not consider so-called "mixture" models, often associated with multi-phase flow, in which the individual species in a computational zone are modeled as fully or partially intermingled. The multi-material cells we consider invariably arise in multi-material Arbitrary Lagrangian-Eulerian (ALE) methods [13, 23], where the results of Lagrangian hydrodynamics are projected onto a new mesh during the remap phase, thereby making a Lagrangian step with a mixed cell a necessity. We consider three main design principles that govern closure models of interest. The first principle is preservation of contacts; this implies that if all materials in a mixed cell are initially at the same pressure, then that pressure does not change due to the closure model. The second principle is that of pressure equilibration; that is, after some transition time (possibly but not necessarily a single timestep), all pressures in the mixed cell equilibrate. The third principle is the exact conservation of total energy. We assume that a separate set of material properties is maintained for each material in every multi-material cell, together with the materials' volume fractions, which can be used to reconstruct material interfaces inside a mixed cell. The main challenge is to accurately assign the thermodynamic states of the individual material components together with the nodal forces that such a zone generates, pursuant to our design principles and despite a lack of detailed information about the velocity distribution within such cells. In particular, for the calculation of both the equation of state (EOS) and the resulting pressure forces, it is important that the calculation of the internal energy be accurate.

There are several existing models for this problem. In one class of methods (see, e.g., Barlow [4], Delov & Sadchikov [9], Goncharov & Yanilkin [11]), one estimates the velocity normal to the interface between materials and then approximates the change in the volume for each material, with internal energy updated separately for each material from its own $pdV$ equation. A common pressure for a mixed cell, which is used in the momentum equation, is computed using the equation of total energy conservation. Delov & Sadchikov [9] and Goncharov & Yanilkin [11] introduce an exchange of internal energy between the materials inside a mixed cell, thereby allowing some freedom in the definition of the common pressure. Other multi-material models impose either instantaneous pressure equilibration (such as that of Lagoutière [18] and Després & Lagoutière [10]) or ascribe an implicit mechanism for pressure relaxation (such as described by Tipton [30] and summarized by Shashkov [28]).

We restrict our attention to the approach in which the change in heat in the constituent materials in the mixed cell is posited to be equal, following Lagoutière [18] and Després & Lagoutière [10]. Under this assumption, the mixed-cell model can be cast as four equations in four unknowns, consisting of the updated values of the specific internal energy and the specific volume for each of the two materials in the mixed cell. A solution to this

set of nonlinear equations can be obtained, e.g., with Newton's method, which forms one element of an overall predictor-corrector scheme for solving the governing conservation laws.

An unsatisfactory aspect of this model, however, is the imposition of instantaneous pressure equilibration among the mixed-cell constituents. We break this assumption using a sub-cell dynamics model based on a local Riemann problem. Specifically, the unique contribution of our work is the development of this physics-inspired, geometry-based approach, using an optimization framework, both (i) to break instantaneous pressure equilibration by relaxing the individual sub-cell pressures to equilibrium and (ii) to determine the single updated value of the relaxing-toward-equilibrium pressure assigned to the overall mixed cell. This approach couples the problem of assigning a single mixed-cell pressure to the physics associated with the local dynamical evolution. We discuss several test problems, using either ideal-gas or stiffened-gas equations of state, on which we exercise this method, providing complete details of the setup for each problem together with qualitative and quantitative results of our approach on these problems.

This paper is structured as follows. Section 2 describes the basic 1-D Lagrangian hydrodynamics equations and the predictor-corrector scheme we employ to obtain solutions. We describe details of the two-material model, based on the work of Lagoutière [18] and Després & Lagoutière [10], in Section 3. Extensions of this model to account for relaxation through the dynamics of a sub-cell Riemann problem are discussed in Section 4, which also contains a brief description of Tipton's method. A specification of test problems and results for this method is provided in Section 5, which also contains comparisons with results for Tipton's method and pure-material calculations. We summarize our findings and conclude in Section 6.

## 2   One-dimensional Lagrangian hydrodynamics

In this section, we describe the basic predictor-corrector algorithm that we use to obtain numerical solutions to the governing equations discussed in the previous section. We first restrict our attention to the single-material case, then discuss where modifications for multi-material cells are required.

The partial differential equations governing the conservation of momentum and internal energy, written in the Lagrangian frame of reference, are (discussed, e.g., by Caramana et al. [7]):

$$\rho \frac{du}{dt} + \nabla P = 0, \tag{2.1}$$

$$\rho \frac{d\varepsilon}{dt} + P \nabla \cdot u = 0. \tag{2.2}$$

In these equations, $u$ is the velocity and $P = P(\tau, \varepsilon)$ is the thermodynamic pressure, where $\varepsilon$ is the specific internal energy (SIE) and $\tau$ is the specific volume, which is given by the

inverse of the mass density $\rho$ of the fluid. In standard Lagrangian methods, the mass of a fluid parcel is constant, so that $\tau$ can be expressed as the volume of that parcel divided by its mass. In this section, subscripts denote spatial position and superscripts indicate temporal indexing. In our staggered-mesh discretization, cell-centers (at index $i+1/2$) are associated with cell masses $M_{i+1/2}$, cell volumes $V_{i+1/2}$, and thermodynamic state variables of the cell, such as density $\rho_{i+1/2}$, specific volume $\tau_{i+1/2}$, SIE $\varepsilon_{i+1/2}$, pressure $p_{i+1/2}$, and sound speed $cs_{i+1/2}$. The vertices of cell $i$ are associated with edge positions $x_i$ and $x_{i+1}$, edge velocities $u_i$ and $u_{i+1}$, and node-centered control volume masses $m_i$ and $m_{i+1}$. The volumes are determined from the edge positions, which evolve according to the trajectory equation,

$$\frac{dx_i}{dt} = u_i. \tag{2.3}$$

We assume that we have all the necessary information to completely specify the values of all state variables at time $t^n$ and seek to update the solution to time $t^{n+1} \equiv t^n + \delta t$, where $\delta t$ is the timestep chosen to satisfy necessary stability requirements (e.g., the CFL condition). The following set of coupled, implicit equations captures the dynamics of the one-dimensional conservation equations by linking the updated values of the flow field with the current state:

$$m_i \frac{u_i^{n+1} - u_i^n}{\delta t} = -\Delta\left(\frac{p_i^n + p_i^{n+1}}{2}\right), \tag{2.4}$$

$$u_i^{n+1/2} = \frac{1}{2}\left(u_i^n + u_i^{n+1}\right), \tag{2.5}$$

$$x_i^{n+1} = x_i^n + \delta t \cdot u_i^{n+1/2}, \tag{2.6}$$

$$V_{i+1/2}^{n+1} = x_{i+1}^{n+1} - x_i^{n+1}, \tag{2.7}$$

$$\tau_{i+1/2}^{n+1} = V_{i+1/2}^{n+1}/M_{i+1/2}, \tag{2.8}$$

$$M_{i+1/2} \frac{\varepsilon_{i+1/2}^{n+1} - \varepsilon_{i+1/2}^n}{\delta t} = -\left(\frac{p_{i+1/2}^n + p_{i+1/2}^{n+1}}{2}\right)\Delta^* u_{i+1/2}^{n+1/2}, \tag{2.9}$$

$$p_{i+1/2}^{n+1} = \mathcal{P}(\tau_{i+1/2}^{n+1}, \varepsilon_{i+1/2}^{n+1}). \tag{2.10}$$

Here, $\mathcal{P}$ is the relation that gives the pressure as a function of the density and SIE. Also, the operator $\Delta$ and its adjoint $\Delta^*$ are defined on the appropriate discrete function spaces as:

$$\Delta\xi_i \equiv \xi_{i+1/2} - \xi_{i-1/2}, \tag{2.11}$$

$$\Delta^*\eta_{i+1/2} \equiv \eta_{i+1} - \eta_i. \tag{2.12}$$

We propose the following iterative scheme by which to obtain a solution for the variables at $t^{n+1}$ in Eqs. (2.4)-(2.10):

Set

$$p_{i+1/2}^{n+1,0} := p_{i+1/2}^n \tag{2.13}$$

and iterate for $s = 1, \cdots$:

$$m_i \frac{u_i^{n+1,s} - u_i^n}{\delta t} = -\Delta \left( \frac{p_i^n + p_i^{n+1,s-1}}{2} \right), \tag{2.14}$$

$$u_i^{n+1/2,s} = \frac{1}{2} \left( u_i^n + u_i^{n+1,s} \right), \tag{2.15}$$

$$x_i^{n+1,s} = x_i^n + \delta t \cdot u_i^{n+1/2,s}, \tag{2.16}$$

$$V_{i+1/2}^{n+1,s} = x_{i+1}^{n+1,s} - x_i^{n+1,s}, \tag{2.17}$$

$$\tau_{i+1/2}^{n+1,s} = V_{i+1/2}^{n+1,s} / M_{i+1/2}, \tag{2.18}$$

$$M_{i+1/2} \frac{\varepsilon_{i+1/2}^{n+1,s} - \varepsilon_{i+1/2}^n}{\delta t} = - \left( \frac{p_{i+1/2}^n + p_{i+1/2}^{n+1,s-1}}{2} \right) \Delta^* u_{i+1/2}^{n+1/2,s}, \tag{2.19}$$

$$p_{i+1/2}^{n+1,s} = \mathcal{P}(\tau_{i+1/2}^{n+1,s}, \varepsilon_{i+1/2}^{n+1,s}). \tag{2.20}$$

As shown by Bauer et al. [5], this iteration is stable under the usual constraints, e.g., CFL number between zero and one. Moreover, this scheme is nominally second order accurate in both space and time for sufficiently smooth initial conditions and sufficiently short times; the method invariably degenerates to first order as discontinuous flow features develop.

One can interpret the first two iterations of this algorithm as a predictor-corrector method. Indeed, each of these steps conserves momentum and total energy. We write the resulting numerical scheme as follows:

---

*Predictor*

$$m_i \frac{u_i^{n+1,\star} - u_i^n}{\delta t} = -\Delta p_i^n, \tag{2.21}$$

$$\Rightarrow \quad u_i^{n+1,\star} = u_i^n - \frac{\delta t}{m_i} \left( p_{i+1/2}^n - p_{i-1/2}^n \right), \tag{2.22}$$

$$u_i^{n+1/2,\star} = \frac{1}{2} \left( u_i^n + u_i^{n+1,\star} \right), \tag{2.23}$$

$$x_i^{n+1,\star} = x_i^n + \delta t \cdot u_i^{n+1/2,\star}, \tag{2.24}$$

$$V_{i+1/2}^{n+1,\star} = x_{i+1}^{n+1,\star} - x_i^{n+1,\star}, \tag{2.25}$$

$$\tau_{i+1/2}^{n+1,\star} = V_{i+1/2}^{n+1,\star} / M_{i+1/2}, \tag{2.26}$$

$$M_{i+1/2} \frac{\varepsilon_{i+1/2}^{n+1,\star} - \varepsilon_{i+1/2}^n}{\delta t} = -p_{i+1/2}^n \Delta^* u_{i+1/2}^{n+1/2,\star}, \tag{2.27}$$

$$\Rightarrow \quad \varepsilon_{i+1/2}^{n+1,\star} = \varepsilon_{i+1/2}^n - \frac{\delta t}{M_{i+1/2}} p_{i+1/2}^n \left( u_{i+1}^{n+1/2,\star} - u_i^{n+1/2,\star} \right), \tag{2.28}$$

$$p_{i+1/2}^{n+1,\star} = \mathcal{P}(\tau_{i+1/2}^{n+1,\star}, \varepsilon_{i+1/2}^{n+1,\star}). \tag{2.29}$$

*Corrector*

$$m_i \frac{u_i^{n+1} - u_i^n}{\delta t} = -\Delta\left(\frac{p_i^n + p_i^{n+1,\star}}{2}\right), \tag{2.30}$$

$$\Rightarrow \quad u_i^{n+1} = u_i^n - \frac{1}{2}\frac{\delta t}{m_i}\left(p_{i+1/2}^n + p_{i+1/2}^{n+1,\star} - p_{i-1/2}^n - p_{i-1/2}^{n+1,\star}\right), \tag{2.31}$$

$$u_i^{n+1/2} = \frac{1}{2}\left(u_i^n + u_i^{n+1}\right), \tag{2.32}$$

$$x_i^{n+1} = x_i^n + \delta t \cdot u_i^{n+1/2}, \tag{2.33}$$

$$V_{i+1/2}^{n+1} = x_{i+1}^{n+1} - x_i^{n+1}, \tag{2.34}$$

$$\tau_{i+1/2}^{n+1} = V_{i+1/2}^{n+1}/M_{i+1/2}, \tag{2.35}$$

$$M_{i+1/2}\frac{\varepsilon_{i+1/2}^{n+1} - \varepsilon_{i+1/2}^n}{\delta t} = -\left(\frac{p_{i+1/2}^n + p_{i+1/2}^{n+1,\star}}{2}\right)\Delta^* u_{i+1/2}^{n+1/2}, \tag{2.36}$$

$$\Rightarrow \quad \varepsilon_{i+1/2}^{n+1} = \varepsilon_{i+1/2}^n - \frac{1}{2}\frac{\delta t}{M_{i+1/2}}\left(p_{i+1/2}^n + p_{i+1/2}^{n+1,\star}\right)\left(u_{i+1}^{n+1/2} - u_i^{n+1/2}\right), \tag{2.37}$$

$$p_{i+1/2}^{n+1} = \mathcal{P}(\tau_{i+1/2}^{n+1}, \varepsilon_{i+1/2}^{n+1}). \tag{2.38}$$

This predictor-corrector scheme can be made more efficient and equally as accurate (at least formally) by replacing the EOS call in Eq. (2.29) with a predictor pressure assignment based on an adiabatic relation among pressure, density, and SIE. In this case, we replace Eq. (2.29) by:

$$p_{i+1/2}^{n+1,\star} = p_{i+1/2}^n - \frac{(cs_{i+1/2}^n)^2}{\tau_{i+1/2}^n}\frac{\delta V_{i+1/2}^{n+1,\star}}{V_{i+1/2}^n}, \tag{2.39}$$

where $\delta V_{i+1/2}^{n+1,\star} \equiv V_{i+1/2}^{n+1,\star} - V_{i+1/2}^n$. One must, however, retain the full EOS call in the corrector step of Eq. (2.38), to ensure thermodynamic consistency and conservation at the updated time.

To decrease non-physical results for problems with discontinuous solutions (e.g., shockwaves), the pressure in these expressions can be augmented by an artificial viscosity to provide additional numerical dissipation. In practice, we modify each occurrence of the pressure $p$ in the above approach by adding an additional term $q$: notionally, $p_{i+1/2} \leftarrow p_{i+1/2} + q_{i+1/2}$ in Eqs. (2.4), (2.9), etc. For example, to calculate the artificial viscosity $q_{i+1/2}^n$ at cell centers at $t^n$, used in Eqs. (2.22) and (2.28), the classical linear-plus-quadratic model of von Neumann & Richtmyer [24] (see also Landshoff [19]), active only in compression, is evaluated as:

$$q_{i+1/2}^n = \begin{cases} 0, & \text{if } u_{i+1}^n - u_i^n \geq 0, \\ -\nu_1 \rho_{i+1/2}^n cs_{i+1/2}^n (u_{i+1}^n - u_i^n) + \nu_2 \rho_{i+1/2}^n (u_{i+1}^n - u_i^n)^2, & \text{otherwise,} \end{cases} \tag{2.40}$$
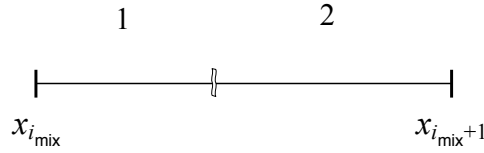
Figure 1: Schematic of the idealized mixed cell, which has material 1 (to the left) separated from material 2 (to the right).

where $\nu_1$ (numerically, nominally $\sim 1$) and $\nu_2$ ($\sim 0.1$) are the coefficients of the linear and quadratic contributions, respectively, and $\rho_{i+1/2}^n \equiv 1/\tau_{i+1/2}^n$. Similar expressions apply to predictor values of artificial viscosity, used, e.g., in Eqs. (2.31) and (2.37). While more sophisticated artificial viscosity models are available (as described, e.g., by Campbell & Shashkov [6]), the simple linear-plus-quadratic model is sufficient to demonstrate the efficacy of the numerical methods for the 1-D gasdynamics problems discussed here.

## 3  Two-material instantaneous equilibrium model

We now examine a specific instantaneous pressure equilibrium model for a two-material mixed cell. We make the fundamental assumption that the fluids are not intermingled; that is, we assume that there is a scale on which the two fluids are separated. We first review the model based on the work of Lagoutière [18] and Després & Lagoutière [10], in which the overall specific volume and SIE in a mixed cell are distributed to the separate materials, and discuss how to use this model with the above algorithm.

A schematic of the mixed cell is shown in Fig. 1, which indicates material 1 to the left of an idealized (massless) interface, which separates it from material 2 to the right. In the following discussion, we largely suppress the subscript index of the mixed cell, $i_{\text{mix}}$; instead, subscripts refer to the two materials in the multi-material cell. In keeping with the single-material algorithm discussed in the previous section, assume that we have the following quantities, consistently updated to time $t^{n+1}$:

1. $\tau^{n+1}$: the updated value of the overall specific volume of the mixed cell, from Eqs. (2.26) and (2.35); and

2. $\varepsilon^{n+1}$: the updated value of the overall SIE of the mixed cell, from Eqs. (2.28) and (2.37).

We also know a common pressure at the previous timestep, $p^n$, for the mixed cell; we discuss later how to update this common pressure from the constituent materials' updated pressures. In addition to those values, we know the specific volume and SIE of the mixed cell's constituent materials at the previous timestep, i.e., $\tau_1^n, \tau_2^n, \varepsilon_1^n, \varepsilon_2^n$.

The quantities that we seek are the updated values of these properties, viz.,

1. $\tau_1^{n+1}, \tau_2^{n+1}$: the updated specific volumes of materials 1 and 2, and

2. $\varepsilon_1^{n+1}, \varepsilon_2^{n+1}$: the updated SIEs of materials 1 and 2,

to be apportioned in some conservative fashion. With these values, the individual materials' EOSs define the associated thermodynamic variables. In the mixed cell, denote the mass fractions ("concentrations") by $c_1$ and $c_2$ for materials 1 and 2, respectively:

$$c_1 = m_1 / M_{i_{\text{mix}}} \quad \text{and} \quad c_2 = m_2 / M_{i_{\text{mix}}}, \tag{3.1}$$

where in the mixed cell

$$m_1 = \text{mass of material 1}, \quad m_2 = \text{mass of material 2}, \tag{3.2}$$
$$M_{i_{\text{mix}}} = \text{total mass} = m_1 + m_2. \tag{3.3}$$

Since the masses in the Lagrangian cells are fixed, the mass fractions $c_1$ and $c_2$ do not vary with time.

The governing equations of the closure model discussed by Lagoutière [18] and Després & Lagoutière [10] are the following.

- Conservation of mass (expressed with the specific volume):

$$c_1 \tau_1^{n+1} + c_2 \tau_2^{n+1} = \tau^{n+1}. \tag{3.4}$$

- Conservation of internal energy (expressed with the SIE):

$$c_1 \varepsilon_1^{n+1} + c_2 \varepsilon_2^{n+1} = \varepsilon^{n+1}. \tag{3.5}$$

- Equality of change in heat of the two materials: with $dQ_k = d\varepsilon_k + P_k dV_k$, this requirement implies:

$$\varepsilon_1^{n+1} - \varepsilon_1^n + P_1(\tau_1^{n+1} - \tau_1^n) = \varepsilon_2^{n+1} - \varepsilon_2^n + P_2(\tau_2^{n+1} - \tau_2^n). \tag{3.6}$$

- Equality of thermodynamic pressure $\mathcal{P}_k(\tau, \varepsilon)$ of the two materials ($k = 1, 2$):[†]

$$p = p_1^{n+1} = p_2^{n+1} \quad \Rightarrow \quad \mathcal{P}_1(\tau_1^{n+1}, \varepsilon_1^{n+1}) - \mathcal{P}_2(\tau_2^{n+1}, \varepsilon_2^{n+1}) = 0. \tag{3.7}$$

The four relations (3.4), (3.5),[‡] (3.6), and (3.7) form a set of four nonlinear equations in four unknowns: $\tau_1^{n+1}$, $\varepsilon_1^{n+1}$, $\tau_2^{n+1}$, and $\varepsilon_2^{n+1}$.

A choice must be made in how to model the pressure in Eq. (3.6). Among the obvious options are the following (where $k = 1, 2$ for the two materials):

- "Fully Implicit": $P_k = p_k^{n+1}$, the pressure at the updated time;
- "Fully Explicit": $P_k = p_k^n$, the pressure at the previous time; or
- "Thermodynamically Consistent": $P_k = \frac{1}{2}(p_k^n + p_k^{n+1})$, the arithmetic mean of the previous-time and updated-time pressures.

---

[†]This relation explicitly specifies the common pressure of the mixed cell.
[‡]As explained by Després & Lagoutière [10], Eqs. (3.4) and (3.5) are consistent with the assumption that the fluids are separated at some scale.

For a polytropic gas, closed-form solutions of this set of equations can be obtained in each of these three cases. Kamm & Shashkov [17] provide explicit expressions for these solutions, which, though algebraically complicated, can be used to verify the software implementation of this algorithm. For general EOSs, Eqs. (3.4)-(3.7) do not admit a closed-form solution, whether one considers the fully implicit, fully explicit, or thermodynamically consistent closure models. In this case, Newton's method can be used to obtain numerical solution to this set of coupled nonlinear equations.

# 4  Two-material Riemann problem/pressure relaxation model

The model of the previous section provides an approach in which the pressures of the constituents of a two-material cell are equilibrated at the end of each timestep. In this section, we describe a sub-cell dynamics model that leads to schemes by which to relax the constituent pressures to equilibrium. That is, given an initial state with a discrepancy between the pressures of material 1 and material 2, we seek a model with which to update material pressures $p_1^{n+1}$ and $p_2^{n+1}$ such that the difference between these values approaches zero as time increases.[§] We do so with a purely dynamical model that does not appeal to any explicit dissipation terms, per se.

Conceptually, we posit a relaxation operator $\mathcal{R}$ that takes as input the thermodynamic states of the constituent materials at time $t^n$ together with values for the overall specific volume and SIE at time $t^{n+1}$. On output, this operator returns the thermodynamic states of the individual materials updated to time $t^{n+1}$ and an estimate of an updated common cell pressure. Schematically, we write this as:

$$\mathcal{R}\left(\tau_1^n,\varepsilon_1^n,\tau_2^n,\varepsilon_2^n;\tau^{n+1},\varepsilon^{n+1}\right)=\left\{\tau_1^{n+1},\varepsilon_1^{n+1},\tau_2^{n+1},\varepsilon_2^{n+1};p^{n+1}\right\}. \tag{4.1}$$

In this section we describe in detail the relaxation operator $\mathcal{R}$.

## 4.1  Two-material Riemann-problem/relaxation model: equations

The foundation of this approach is to consider the evolution of the multi-material cell over one timestep to be related to a local Riemann problem. This cell is identified by the index $i_{\mathrm{mix}}$, with the states of the two materials assumed to be available at time $t^n$. The location of the interface between the materials at this time is determined by the local volume fraction of, say, material 1, given by $f_1$:

$$x_{\mathrm{intfc}}^n = x_{i_{\mathrm{mix}}}^n + f_1\left(x_{i_{\mathrm{mix}}+1}^n - x_{i_{\mathrm{mix}}}^n\right) \in \left[x_{i_{\mathrm{mix}}}^n, x_{i_{\mathrm{mix}}+1}^n\right]. \tag{4.2}$$

---

[§]This idealized picture is for the special case of stationary flow, i.e., in the absence of external flow perturbations. More generally, when there are persistent external flow effects one should not expect pressure equilibration in a mixed cell to necessarily obtain.
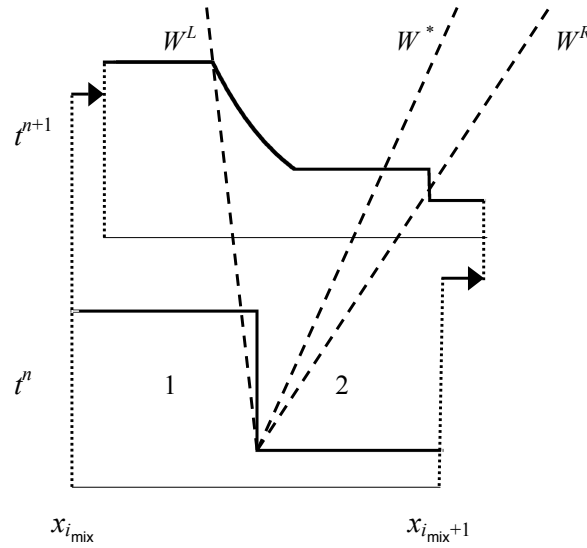
Figure 2: Schematic of the pressure associated with the 1-D Riemann problem used to model the dynamics of the two-material mixed cell. The bottom shows the initial pressure, i.e., at time $t^n$, of materials 1 (left) and 2 (right), while the top figure is the updated solution, i.e., at time $t^{n+1}$. The $t^{n+1}$ state exhibits, from left to right, the left $t^n$ value, the leading left-most Riemann wave ($W^L$, in this case corresponding to a rarefaction fan), the contact discontinuity ($W^*$), the leading right-most Riemann wave ($W^R$, in this case corresponding to a shock), and the right $t^n$ quantity.

In higher dimensions, the interface configuration must be estimated with an interface reconstruction technique. Specifically, the two states in this cell at $t^n$ are given by:

$$(\rho, \varepsilon, p, u) = \begin{cases} (\rho_1, \varepsilon_1, p_1, u_1), & \text{if } x^n_{i_{\text{mix}}} < x < x^n_{\text{intfc}}, \\ (\rho_2, \varepsilon_2, p_2, u_2), & \text{if } x^n_{\text{intfc}} < x < x^n_{i_{\text{mix}}+1}. \end{cases} \tag{4.3}$$

There is an obvious choice for the velocities in 1-D, viz.,

$$u_1 = u_{i_{\text{mix}}} \qquad \text{and} \qquad u_2 = u_{i_{\text{mix}}+1}. \tag{4.4}$$

More sophisticated models that involve spatial variation of the velocity could be used, but we use this piecewise-constant assumption in the following. The solution to this one-cell Riemann problem at time $t^{n+1}$ can be computed for polytropic gases according to the method of Gottlieb & Groth [12], for stiffened gases following Plohr [25], and for more general equations of state as described by Colella & Glaz [8] and Quartapelle et al. [26].

A schematic of the initial conditions and idealized solution to this problem is shown in Fig. 2, which depicts the pressure for the mixed cell at $t^n$ on the bottom and at $t^{n+1}$ on the top, in the particular case of a rarefaction-contact-shock configuration. In this figure, the top ($t^{n+1}$) diagram exhibits, from left to right, the left $t^n$ state, the leading left-most Riemann wave ($W^L$), the contact discontinuity ($W^*$), the leading right-most Riemann

wave ($W^R$), and the right $t^n$ state. The states outside of the leading waves are unchanged from their values at $t^n$ during the timestep $\delta t$. If the left- or right-most wave is a shock, then the precise location of this wave is unambiguous; if this wave is a rarefaction, however, then we do not use the exact solution but instead choose either the head or tail of the rarefaction as defining the location of this wave (as in Fig. 2). In the domains delimited by these waves, i.e., between the left-most wave and the contact, and between the contact and the right-most wave, we assume the Riemann-problem pressure is constant in space at time $t^{n+1}$; outside these waves, we assume that the pressure retains its initial (i.e., at $t^n$) values. Depending on the initial conditions of the Riemann problem, these assumptions may not be strictly valid (e.g., when rarefactions are present); nonetheless, they can be used in the optimization method that we describe below.[¶]

Let the region to the left of the contact contain two sets $\Omega_1$ and $\Omega_2$, defined as

$$\Omega_1 \equiv \left\{ x : x_{i_{\mathrm{mix}}}^{n+1} < x < x_{\mathrm{left}}^{\mathrm{RP}} \right\} \quad \text{and} \quad \Omega_2 \equiv \left\{ x : x_{\mathrm{left}}^{\mathrm{RP}} < x < x_{\mathrm{cont}}^{\mathrm{RP}} \right\}, \tag{4.5}$$

where $x_{\mathrm{left}}^{\mathrm{RP}}$ is the position of the left-most wave $W^L$ and $x_{\mathrm{cont}}^{\mathrm{RP}}$ is the contact position, both determined from the solution to the Riemann problem (identified by the superscript "RP"). Denote similar subsets to the right of the contact as $\Omega_3$ and $\Omega_4$:

$$\Omega_3 \equiv \left\{ x : x_{\mathrm{cont}}^{\mathrm{RP}} < x < x_{\mathrm{right}}^{\mathrm{RP}} \right\} \quad \text{and} \quad \Omega_4 \equiv \left\{ x : x_{\mathrm{right}}^{\mathrm{RP}} < x < x_{i_{\mathrm{mix}}+1}^{n+1} \right\}, \tag{4.6}$$

where $x_{\mathrm{right}}^{\mathrm{RP}}$ is the position of the right-most wave $W^R$ of the Riemann problem solution.

The key assumption of our approach is the following: we seek a single updated pressure value for each material (i.e., on each side of the contact) that minimizes the discrepancy between that value and the pressure given by the Riemann problem solution in that domain. A mathematical expression of this statement replaces the instantaneous pressure equilibration equation (i.e., Eq. (3.7)) while the other constraints of the model (Eqs. (3.4)-(3.6)) still apply.

We express this relation mathematically as the following optimization problem:

$$\min_{\{\tau_1^{n+1}, \varepsilon_1^{n+1}, \tau_2^{n+1}, \varepsilon_2^{n+1}\}} \left( ||p_1^{n+1} - p_1^{\mathrm{RP}}||^2 + ||p_2^{n+1} - p_2^{\mathrm{RP}}||^2 \right) \tag{4.7}$$

subject to the constraints given by Eqs. (3.4)-(3.6):

$$\mathcal{F}_1 \equiv c_1 \tau_1^{n+1} + c_2 \tau_2^{n+1} - \tau^{n+1} = 0, \tag{4.8}$$

$$\mathcal{F}_2 \equiv c_1 \varepsilon_1^{n+1} + c_2 \varepsilon_2^{n+1} - \varepsilon^{n+1} = 0, \tag{4.9}$$

$$\mathcal{F}_3 \equiv \varepsilon_1^{n+1} - \varepsilon_1^n + P_1(\tau_1^{n+1} - \tau_1^n)$$
$$- \left[ \varepsilon_2^{n+1} - \varepsilon_2^n + P_2(\tau_2^{n+1} - \tau_2^n) \right] = 0. \tag{4.10}$$

---

[¶]One could utilize the entire non-piecewise-constant solution pressure when a rarefaction fan is present. Such a model introduces additional complexity to the relaxation model presented below.

In Eq. (4.7), $p_1^{\text{RP}}$ and $p_2^{\text{RP}}$ are the pressures, in materials 1 and 2, related to the solution of the Riemann problem. These pressure values are constant on the subsets $\Omega_j$, $j=1,\cdots,4$; as described above, they differ from the exact Riemann problem solution only across a rarefaction, through which a constant value is assumed.

Using the $L_2$ norm, the components of the expression in Eq. (4.7) can be written in terms of the locally constant pressure values in each domain:

$$||p_1^{n+1}-p_1^{\text{RP}}||^2 = \tilde{\Omega}_1\left(p_1^{n+1}-p_1^{\text{RP}}\right)^2 + \tilde{\Omega}_2\left(p_1^{n+1}-p_1^{\text{RP}}\right)^2, \tag{4.11}$$

$$||p_2^{n+1}-p_2^{\text{RP}}||^2 = \tilde{\Omega}_3\left(p_2^{n+1}-p_2^{\text{RP}}\right)^2 + \tilde{\Omega}_4\left(p_2^{n+1}-p_2^{\text{RP}}\right)^2. \tag{4.12}$$

Here, the nondimensional quantity $\tilde{\Omega}_j$ equals the measure of the set $\Omega_j$ divided by the entire cell length, $\delta x^{n+1}$:

$$\tilde{\Omega}_j = \left(\max_{x\in\Omega_j} x - \min_{x\in\Omega_j} x\right) \Big/ \left(x_{i_{\text{mix}}+1}^{n+1} - x_{i_{\text{mix}}}^{n+1}\right); \tag{4.13}$$

with this definition,

$$\tilde{\Omega}_j \geq 0, \ \forall j, \quad \text{and} \quad \sum_{j=1}^{4}\tilde{\Omega}_j = 1. \tag{4.14}$$

Outside of the leading waves, i.e., on sets $\Omega_1$ and $\Omega_4$, the Riemann problem pressure equals the pressure at the start of the timestep:

$$p_1^{\text{RP}} = p_1^n \ \text{for} \ x\in\Omega_1 \quad \text{and} \quad p_2^{\text{RP}} = p_2^n \ \text{for} \ x\in\Omega_4. \tag{4.15}$$

Between the contact and these waves, we assign the pressure to be the so-called "star-state" pressure of the Riemann problem solution, described, e.g., by Toro [31] and LeVeque [20]:

$$p_1^{\text{RP}} = p^* \ \text{for} \ x\in\Omega_2 \quad \text{and} \quad p_2^{\text{RP}} = p^* \ \text{for} \ x\in\Omega_3. \tag{4.16}$$

Therefore, Eqs. (4.11) and (4.12) imply the following relations:

$$||p_1^{n+1}-p_1^{\text{RP}}||^2 = \tilde{\Omega}_1\left(p_1^{n+1}-p_1^n\right)^2 + \tilde{\Omega}_2\left(p_1^{n+1}-p^*\right)^2, \tag{4.17}$$

$$||p_2^{n+1}-p_2^{\text{RP}}||^2 = \tilde{\Omega}_3\left(p_2^{n+1}-p^*\right)^2 + \tilde{\Omega}_4\left(p_2^{n+1}-p_2^n\right)^2. \tag{4.18}$$

We recast this constrained minimization problem as simple minimization through the use of Lagrange multipliers. Specifically, to the expression to be minimized we add each of the constraint terms multiplied by an unknown parameter (the Lagrange multiplier) and then seek to minimize that composite function. The overall minimization statement then becomes the following:

$$\min_{\{\tau_1^{n+1},\varepsilon_1^{n+1},\tau_2^{n+1},\varepsilon_2^{n+1},\lambda_1,\lambda_2,\lambda_3\}} \mathcal{G}\left(\tau_1^{n+1},\varepsilon_1^{n+1},\tau_2^{n+1},\varepsilon_2^{n+1},\lambda_1,\lambda_2,\lambda_3\right) \tag{4.19}$$

where

$$\mathcal{G} \equiv ||p_1^{n+1} - p_1^{\mathrm{RP}}||^2 + ||p_2^{n+1} - p_2^{\mathrm{RP}}||^2 + \lambda_1 \mathcal{F}_1 + \lambda_2 \mathcal{F}_2 + \lambda_3 \mathcal{F}_3. \tag{4.20}$$

A possible extremum of the function $\mathcal{G}$ is obtained by finding a solution that corresponds to a zero of the coupled set of nonlinear equations given by:

$$\partial \mathcal{G} / \partial X_i = 0, \; i = 1, \cdots, 7, \quad \text{where} \quad \boldsymbol{X} \equiv \left[ \tau_1^{n+1}, \varepsilon_1^{n+1}, \tau_2^{n+1}, \varepsilon_2^{n+1}, \lambda_1, \lambda_2, \lambda_3 \right]^{\mathrm{T}}. \tag{4.21}$$

Since the derivative of $\mathcal{G}$ with respect to a Lagrange multipliers is just the corresponding constraint equation, parameter values that satisfy $\partial \mathcal{G} / \partial X_i = 0$ perforce obey the constraint equations. Numerical solutions to this problem can be sought with Newton's method for the system of equations given in Eq. (4.21).

In practice, the terms in the objective function $\mathcal{G}$ are nondimensionalized by local representative values, so that the contributions to $\mathcal{G}$ are roughly comparable. One such nondimensionalization is:

$$\begin{aligned}
\mathcal{G} \equiv{}& \tilde{\Omega}_1 \left( p_1^{n+1} - p_1^n \right)^2 / \bar{p}^2 + \tilde{\Omega}_2 \left( p_1^{n+1} - p^* \right)^2 / \bar{p}^2 \\
&+ \tilde{\Omega}_3 \left( p_2^{n+1} - p^* \right)^2 / \bar{p}^2 + \tilde{\Omega}_4 \left( p_2^{n+1} - p_2^n \right)^2 / \bar{p}^2 \\
&+ \lambda_1 \left[ (c_1 \tau_1^{n+1} + c_2 \tau_2^{n+1}) - \tau^{n+1} \right] / \bar{\tau} + \lambda_2 \left[ (c_1 \varepsilon_1^{n+1} + c_2 \varepsilon_2^{n+1}) - \varepsilon^{n+1} \right] / \bar{\varepsilon} \\
&+ \lambda_3 \left\{ \left[ \varepsilon_1^{n+1} - \varepsilon_1^n + P_1 (\tau_1^{n+1} - \tau_1^n) \right] - \left[ \varepsilon_2^{n+1} - \varepsilon_2^n + P_2 (\tau_2^{n+1} - \tau_2^n) \right] \right\} / \bar{\varepsilon},
\end{aligned} \tag{4.22}$$

where $\bar{p}$, $\bar{\tau}$, and $\bar{\varepsilon}$ are representative (non-zero) values of the pressure, specific volume, and SIE, respectively, of the entire zone at $t^n$ (e.g., $p_{i_{\mathrm{mix}}}^n$, etc.). The properties of the individual constituents that result from this minimization process are used to define the common cell pressure, which we discuss in the next section.

## 4.2 Relaxation to a single pressure

Unlike the instantaneous pressure equilibration model, this approach does *not* imply an unambiguous value for the pressure of the mixed cell. Consistent with the solution of the set of coupled model equations, one could assign the overall mixed-cell pressure value as a spatial average of the two updated pressures:

$$p_{i_{\mathrm{mix}}}^{n+1} = \bar{p} = (\tilde{\Omega}_1 + \tilde{\Omega}_2) p_1^{n+1} + (\tilde{\Omega}_3 + \tilde{\Omega}_4) p_2^{n+1}. \tag{4.23}$$

Alternatively, one could use the information from the sub-cell dynamical evolution model to assign a single pressure to the mixed cell pressure based on the extent of the wave propagation in the associated Riemann problem:

$$p_{i_{\mathrm{mix}}}^{n+1} = \tilde{p} = \tilde{\Omega}_1 p_1^n + (\tilde{\Omega}_2 + \tilde{\Omega}_3) p^* + \tilde{\Omega}_4 p_2^n. \tag{4.24}$$

These values enter into the overall algorithm in Eqs. (2.22), (2.28), (2.31), and (2.37). In the results of Section 5, the common pressure given in Eq. (4.23) is used. For the test problems examined, the difference in results between these two definitions of the common pressure is minor.

To motivate heuristically why this approach leads to pressure equilibration with increasing time, we consider the structure of the Riemann problem solutions. For polytropic gases, the four non-degenerate Riemann problem solution configurations can be denoted, following Gottlieb & Groth [12], as RCS, RCR, SCR, and SCS, where the order corresponds to the wave family from left to right, and the letter identifies the particular wave: "R" means a rarefaction fan, "C" denotes a contact (across which the pressure equals the star-state value and is continuous), and "S" indicates a shock.[||] There are two cases: (1) the star-state pressure, $p^*$, is bounded by the pressures on the left and right (as happens, e.g, in the case of equal polytropic indices for the RCS and SCR solutions with no initial velocity) and (2) $p^*$ exceeds the extremal left and right pressures (i.e., $p^*$ is either less than the minimum pressure or greater than the maximum pressure, e.g., in the case of equal polytropic indices for the RCR and SCS solutions with no initial velocity).

Consider the first case and assume that $p_1^n < p^* < p_2^n$ (the case with $p_1^n > p^* > p_2^n$ is similar). For material 1, the result of the minimization process, $p_1^{n+1}$, must be bounded by $p_1^n$ and $p^*$: if it were not, then one could always find a value $\tilde{p}_1^{n+1}$ that would give a smaller value of the convex combination in Eq. (4.17). An analogous argument holds for material 2. Thus, at the end of the timestep we have the ordering,

$$p_1^n < p_1^{n+1} < p^* < p_2^{n+1} < p_2^n.$$

Therefore, the pressure difference at the end of the timestep, $|p_1^{n+1} - p_2^{n+1}|$, is less than the pressure difference at the start of the timestep, $|p_1^n - p_2^n|$, i.e., the pressures are relaxing toward equilibrium.

Consider now the second case and assume, without loss of generality, that $p^* < p_1^n$, $p_2^n$; for the sake of argument, further assume that $p_1^n < p_2^n$. In material 1, the result of the minimization process, $p_1^{n+1}$, must again be bounded by $p_1^n$ and $p^*$, and similarly for material 2:

$$p^* < p_1^{n+1} < p_1^n \quad \text{and} \quad p^* < p_2^{n+1} < p_2^n.$$

Considering possible values of the positive numbers $\tilde{\Omega}_j$ in Eqs. (4.17) and (4.18), it is conceivable that the pressure difference could increase during the timestep (not accounting for the effect of the other constraints). This analysis leads us to conclude that these inequalities alone are insufficient to ensure that the pressures necessarily tend toward equilibrium, i.e., one cannot immediately infer that

$$|p_1^{n+1} - p_2^{n+1}| < |p_1^n - p_2^n|.$$

---

[||]We ignore the vacuum boundary case. Additionally, the fifth case of the polytropic gas Riemann solutions is the degenerate situation in which a vacuum region develops between the opposing rarefaction waves, i.e., RCVCR, in the above notation. The consequences of this situation with respect to pressure equilibration are comparable to those of the RCR case.

Additional special cases are those of a uniformly translating contact and a uniformly propagating shock. The former perforce obeys pressure equilibrium from $t^n$ to $t^{n+1}$, while the latter necessarily maintains pressure non-equilibrium through the timestep.

Therefore, while it is plausible that some initial (i.e., $t^n$) mixed-cell conditions lead to a decrease in pressure difference over the course of a timestep with our model (i.e., relax toward pressure equilibrium), other initial conditions in the mixed-cell lead to the pressure difference between materials 1 and 2 increasing, at least temporarily. This (local) increase in the pressure difference between materials 1 and 2 is evident in some of the mixed-cell pressure time history results of Section 5; see, e.g., Fig. 19. All of the test problems we consider in Section 5, however, lead to pressure equilibrium in the multi-material cell *at late times*. We speculate that the constituent pressures are driven, at late time, to the star-state pressure of a Riemann problem toward which the mixed cell evolves over many cycles. This speculation assumes that there are no other perturbations that enter the cell and drive it from equilibrium (such as occurs, e.g., in the problem of Section 5.4 and evident in Fig. 24). In future work, we plan to perform more rigorous tests of this hypothesis.

## 4.3   2-material Riemann-problem/relaxation model: numerical implementation

The (single) pressure of a (two-material) mixed cell, $p^n_{i_{\mathrm{mix}}}$, where $i_{\mathrm{mix}}$ is the index of the mixed cell, enters into the overall algorithm, influencing the updated velocities at the edges of the mixed cell. Therefore, the manner in which an overall pressure for the multi-material mixed cell is assigned will have a direct impact on the overall results. In the predictor phase, this value enters in the evaluation of the predictor velocity $u^{n+1,\star}_i$ in Eq. (2.22), which influences the cell edges positions in Eq. (2.24), cell volumes in Eq. (2.25), etc., as well as in the predictor SIE in Eq. (2.28). Similarly, in the corrector phase, the cell velocities, edges, volumes, etc., are affected by the predictor value of the sole mixed-cell pressure in Eqs. (2.31)-(2.37). The pressures of the individual constituents in a multi-material cell are used to generate a single, overall pressure for the entire cell. In addition to this value, the updated values of the state of the two materials (viz., the specific volumes and SIEs) must be carried along into the next computational cycle.

We now describe an algorithmic implementation of the mixed cell model. As mentioned earlier, assume that we have, at time $t^n$, a common pressure value, $p^n_{i_{\mathrm{mix}}}$, for the mixed cell as well as the thermodynamic variables for the individual constituents, $\tau^n_1$, $\varepsilon^n_1$, $\tau^n_2$, $\varepsilon^n_2$. In the predictor phase, the steps listed in Eqs. (2.21)-(2.28) are followed exactly, where the common pressure value from the previous timestep, $p^n_{i_{\mathrm{mix}}}$, is used for the mixed cell. After the step in Eq. (2.28), predictor values for the overall mixed cell specific volume and SIE are generated. Instead of the single-material pressure evaluation given in Eq. (2.29), one invokes the mixed-cell model.

The full evaluation of the predictor values for the mixed cell is as follows.

1. Starting with the initial conditions specified by the mixed-cell state at $t^n$, solve the mixed-cell predictor Riemann problem over the timestep $\delta t$, which we represent notionally as $\Re(\tau_1^n, \varepsilon_1^n, \tau_2^n, \varepsilon_2^n; \delta t)$.

2. Use those results to determine the star-state pressure and the extent of wave propagation: $\Re(\tau_1^n, \varepsilon_1^n, \tau_2^n, \varepsilon_2^n; \delta t) \Rightarrow p^*$ and $\tilde{\Omega}_j$, $j = 1, \cdots, 4$ (see Eq. (4.13)); these quantities are used in the evaluation of the pressure-difference expressions in Eqs. (4.17) and (4.18).

3. Obtain a solution of the associated minimization problem, given in Eqs. (4.19) and (4.20), for predictor values of the thermodynamic state of the individual constituents, $\tau_1^{n+1,\star}$, $\varepsilon_1^{n+1,\star}$, $\tau_2^{n+1,\star}$, $\varepsilon_2^{n+1,\star}$, using the values at $t^n$ as an initial guess.

4. Evaluate the predictor component pressures with EOS calls: $p_k^{n+1,\star} = \mathcal{P}(\tau_k^{n+1,\star}, \varepsilon_k^{n+1,\star})$, $k = 1, 2$.

5. Evaluate the predictor common pressure, $p^{n+1,\star}$, according to either Eq. (4.23) or Eq. (4.24).

For the corrector phase, the steps listed in Eqs. (2.30)-(2.37) are followed, where the predictor common pressure value, $p^{n+1,\star}$, is now used for the mixed cell. Instead of the single-material pressure evaluation given in Eq. (2.38), the corrector phase of the mixed-cell model is evaluated.

1. Starting with the initial conditions specified by the mixed-cell state at $t^n$, solve the mixed-cell Riemann problem over the timestep $\delta t$: $\Re(\tau_1^n, \varepsilon_1^n, \tau_2^n, \varepsilon_2^n; \delta t)$.

2. Use the results of this problem to determine the star-state pressure and the extent of wave propagation: $\Re(\tau_1^n, \varepsilon_1^n, \tau_2^n, \varepsilon_2^n; \delta t) \Rightarrow p^*$ and $\tilde{\Omega}_j$, $j = 1, \cdots, 4$ (see Eq. (4.13)), with which one can evaluate terms of the pressure-difference expressions in Eqs. (4.17) and (4.18).

3. Solve the associated minimization problem, given in Eqs. (4.19) and (4.20), for updated values of the thermodynamic state of the individual constituents, $\tau_1^{n+1}$, $\varepsilon_1^{n+1}$, $\tau_2^{n+1}$, $\varepsilon_2^{n+1}$; here, the predictor values of these quantities can be used as an initial guess.

4. Evaluate the corrector component pressures with EOS calls: $p_k^{n+1} = \mathcal{P}(\tau_k^{n+1}, \varepsilon_k^{n+1})$, $k = 1, 2$.

5. Model the final common pressure, $p^{n+1}$, according to either Eq. (4.23) or Eq. (4.24).

## 4.4   Tipton's method for pressure relaxation

In this section, we describe the assumptions and implementation of Tipton's method for pressure relaxation [28, 30]. In Section 5 we compare the results of our approach with those based on Tipton's method. The underlying integrator for our implementation of Tipton's approach is based on a two-step method, in which certain quantities are first updated to the half-timestep level, and then all flow field quantities are updated to the final time. More specifically, half-timestep updates are made for node positions (using the

trajectory equation), as well as cell volumes and cell densities (both based on updated node positions); the half-timestep pressure is evaluated using an adiabatic approximation. The final timestep updates begin with the velocity (updated from the momentum equation using the half-timestep pressures), followed by the position (using the trajectory equation with time-centered velocities), cell volumes and densities (using updated node positions), and the SIE (using the updated $pdV$ work); for consistency, the final pressure is obtained with a full EOS call.

Specifically, this algorithm can be written as follows for pure material cells.

*Half-timestep Update*

$$x_i^{n+1/2} = x_i^n + (\delta t/2)\, u_i^n, \tag{4.25}$$

$$V_{i+1/2}^{n+1/2} = x_{i+1}^{n+1/2} - x_i^{n+1/2}, \tag{4.26}$$

$$\tau_{i+1/2}^{n+1/2} = V_{i+1/2}^{n+1/2} / M_{i+1/2}, \tag{4.27}$$

$$p_{i+1/2}^{n+1/2} = p_{i+1/2}^n - \frac{(cs_{i+1/2}^n)^2}{\tau_{i+1/2}^n}\frac{\delta V_{i+1/2}^{n+1/2}}{V_{i+1/2}^n}. \tag{4.28}$$

*Full-timestep Update*

$$m_i \frac{u_i^{n+1} - u_i^n}{\delta t} = -\Delta\left(p_i^{n+1/2}\right), \tag{4.29}$$

$$\Rightarrow\quad u_i^{n+1} = u_i^n - \frac{\delta t}{m_i}\left(p_{i+1/2}^{n+1/2} - p_{i-1/2}^{n+1/2}\right), \tag{4.30}$$

$$u_i^{n+1/2} = \frac{1}{2}\left(u_i^n + u_i^{n+1}\right), \tag{4.31}$$

$$x_i^{n+1} = x_i^n + \delta t \cdot u_i^{n+1/2}, \tag{4.32}$$

$$V_{i+1/2}^{n+1} = x_{i+1}^{n+1} - x_i^{n+1}, \tag{4.33}$$

$$\tau_{i+1/2}^{n+1} = V_{i+1/2}^{n+1} / M_{i+1/2}, \tag{4.34}$$

$$M_{i+1/2}\left(\varepsilon_{i+1/2}^{n+1} - \varepsilon_{i+1/2}^n\right) = -p_{i+1/2}^{n+1/2}\,\delta V_{i+1/2}^{n+1} \tag{4.35}$$

$$\Rightarrow\quad \varepsilon_{i+1/2}^{n+1} = \varepsilon_{i+1/2}^n - p_{i+1/2}^{n+1/2}\,\delta V_{i+1/2}^{n+1}/M_{i+1/2}, \tag{4.36}$$

$$p_{i+1/2}^{n+1} = \mathcal{P}(\tau_{i+1/2}^{n+1}, \varepsilon_{i+1/2}^{n+1}), \tag{4.37}$$

where $\delta V_{i+1/2}^{n+j} \equiv V_{i+1/2}^{n+j} - V_{i+1/2}^n$ with $j = 1/2$ or 1.

Tipton's multi-material model is based on this two-step scheme. In the following presentation of the multi-material model, subscripts indicate the material identifier, not the cell index. For this algorithm with two materials, there are three unknowns, the first two of which consist of the volume changes of the two materials in the mixed cell at the half-timestep, $\delta V_k^{n+1/2}$, $k = 1,2$. The next assumption of the model introduces the

third unknown as the overall half-timestep pressure, $p^{n+1/2}$, which is the same for all materials and is assumed equal to the sum of the half-timestep pressure for each material and a half-timestep relaxation term for that material:

$$p^{n+1/2} = p_k^{n+1/2} + R_k^{n+1/2}, \quad k=1,2. \tag{4.38}$$

The first term on the RHS of this equation, the half-timestep pressure of the $k$th material, is evaluated with an adiabatic approximation (as in the pure-material half-timestep update of Eq. (4.28)) that includes this material's unknown volume change:

$$p_k^{n+1/2} = p_k^n - \frac{(cs_k^n)^2}{\tau_k^n} \frac{\delta V_k^{n+1/2}}{V_k^n}. \tag{4.39}$$

The second term on the RHS of Eq. (4.38), the relaxation term for the $k$th material, is posited to be of a form evocative of a traditional linear artificial viscosity that also is based this material's unknown volume change:

$$R_k^{n+1/2} = -\frac{cs_k^n}{\tau_k^n} \frac{L^n}{\delta t} \frac{\delta V_k^{n+1/2}}{V_k^n}, \tag{4.40}$$

where $L^n$ is a characteristic length for the mixed cell (typically the overall cell size). To close this model, one enforces that the sum of the (unknown) volume changes of all materials must equal the overall volume change of the mixed cell, $V^{n+1/2}$, which *is* known from a standard the half-timestep update (using the expression in Eq. (4.26) and the overall volume at $t^n$):

$$\delta V_1^{n+1/2} + \delta V_2^{n+1/2} = \delta V^{n+1/2}. \tag{4.41}$$

As was done for the single-material cells in the rest of the half-timestep update, the new volumes and corresponding volume changes can now be computed for each material. To achieve this for a multiple-material cell, one combines the above expressions and writes the governing relations for the mixed cell as the following set of linear equations in the unknowns $\delta V_1^{n+1/2}$, $\delta V_2^{n+1/2}$, and $p^{n+1/2}$:

$$p_k^n - \tilde{B}_k^n \left( \delta V_k^{n+1/2} / V_k^n \right) = p^{n+1/2}, \quad k=1,2, \qquad \delta V_1^{n+1/2} + \delta V_2^{n+1/2} = \delta V^{n+1/2}, \tag{4.42}$$

where

$$\tilde{B}_k^n \equiv \rho_i^n \left[ (cs_k^n)^2 / \tau_k^n \right] [1 + L^n / (cs_k^n \delta t)], \quad k=1,2. \tag{4.43}$$

This linear system of equations has the solution:

$$p^{n+1/2} = \bar{p}^n - \bar{B}^n \frac{\delta V^{n+1/2}}{V^n} \quad \text{and} \quad \delta V_k^{n+1/2} = \frac{V_k^n}{\tilde{B}_k^n} \left[ (p_k^n - \bar{p}^n) + \bar{B}^n \frac{\delta V^{n+1/2}}{V^n} \right], \quad k=1,2, \tag{4.44}$$

where the barred values are the volume-fraction-averaged quantities given by:

$$\bar{p}^n \equiv \sum_{k=1}^{2} \left( \frac{f_k^n p_k^n}{\tilde{B}_k^n} \right) / \sum_{k=1}^{2} \left( \frac{f_k^n}{\tilde{B}_k^n} \right) \quad \text{and} \quad \bar{B}^n \equiv \left[ \sum_{k=1}^{2} \left( \frac{f_k^n}{\tilde{B}_k^n} \right) \right]^{-1}, \tag{4.45}$$

with $f_k \equiv V_k / V$ representing the volume fraction of the $k$th material. Eq. (4.44) for $\delta V_k^{n+1/2}$ indicates that two factors contribute to the volume change in the $k$th material. The first component is the difference between the pressure in the $k$th material and the "averaged" pressure given by $\bar{p}^n$, while the second factor is related to the overall volume change of the entire mixed cell.

The volume of the $k$th material is related to the overall cell volume $V$ via the volume fraction $f_k$, i.e., $V_k = f_k V$. Thus, one can derive the following equation for the change in the volume fraction at the end of the half-timestep:

$$\delta f_k^{n+1/2} = f_k^n \left[ (p_k^n - \bar{p}^n) / \tilde{B}_k^n \right] + f_k^n \left[ (\bar{B}^n / \tilde{B}_k^n) - 1 \right] \left( \delta V^{n+1/2} / V^n \right). \tag{4.46}$$

These relations provide the necessary information at the half-timestep to update values to the end of the timestep. To do so, we invoke the last assumption of this model, namely, that the individual materials' volume changes at $t^{n+1} = t^n + \delta t = t^n + 2 \cdot (\delta t / 2)$ equal twice the half-timestep values:

$$\delta f_k^{n+1} = 2 \delta f_k^{n+1/2}. \tag{4.47}$$

The individual volume fractions are updated according to:

$$f_k^{n+1} = f_k^n + \delta f_k^{n+1}. \tag{4.48}$$

Using these values, the corresponding volumes of each material in the mixed cell are evaluated (using the updated overall cell volume from Eq. (4.33)) :

$$V_k^{n+1} = f_k^{n+1} V^{n+1}, \tag{4.49}$$

along with each material's density and volume change:

$$\rho_k^{n+1} = M_k / V_k^{n+1} \quad \text{and} \quad \delta V_k^{n+1} = V_k^{n+1} - V_k^n. \tag{4.50}$$

As in the overall cell case, the SIE for each material is obtained from the updated $pdV$ work:

$$\varepsilon_k^{n+1} = \varepsilon_k^n - p^{n+1/2} \delta V_k^{n+1} / M_k. \tag{4.51}$$

Lastly, the individual pressures are consistently evaluated with full EOS calls:

$$p_k^{n+1} = \mathcal{P}_k(\tau_k^{n+1}, \varepsilon_k^{n+1}). \tag{4.52}$$

In the actual implementation, one adds an artificial viscosity term (e.g., to Eq. (4.30)), the specific form of which will affect the computed results. Furthermore, one can conceive of modifications to this method, e.g., by altering the relative contribution of the terms in Eq. (4.46) in order to account, say, for the sub-cell interaction of materials having disparate properties (e.g., small volume fractions). Such modifications may change the results for Tipton's method on the test problems, to which we now turn.

# 5   Test problems and results

We examine several different test problems found in the compressible flow literature in order to evaluate the methods described above. We focus on problems with exact solutions, so that we can rigorously compare the quantitative errors associated with different methods. While several test problems exist and are used by the single-material compressible flow algorithm development community (see, e.g., the overview by Liska & Wendroff [21]), fewer problems are available for code verification of multifluid compressible flow (see, e.g., [14,32,33]).

For results of both the Riemann-relaxation and Tipton's methods on the test problems consider, the mesh consists of $N_x$ zones, each of identical dimension $1/(N_x+1)$, with the exception of a single multi-material zone, which is of width $2/(N_x+1)$. In that multi-material zone, the mass and volume fractions are assigned to be consistent with the initial conditions; also, the initial volume fractions are assigned to be consistent with the initial interface between the two materials being located at the geometric center of the cell. We also compare with a pure-material calculation, i.e., with *no* mixed cell, in which all cells are initially the same width; these calculations contain one more cell than the multi-material calculations, so that for pure-material calculations with $N_x+1$ zones, each zone is of width $1/(N_x+1)$, with the multi-material zone of the other methods effectively split into two pure-material zones of equal dimension. There is no need for our method to be used exclusively either with mixed cells that are larger than the non-mixed cells or with the interface in the middle of the mixed cell. We have set up the test problems in the manner described above in order to compare, as closely as possible, to the corresponding pure-material calculations. All problems were run with the same value of CFL constant, equal to 0.25. We have examined the modified Sod problem of Section 5.2 at several different CFL numbers. For values at or less than 0.5, the results appear to be essentially insensitive to the particular CFL value. At some higher values of CFL number, however, numerical instabilities were seen to develop. These instabilities were evident both in calculations with the multi-material zones and in the pure-material calculations. We suspect that the CFL threshold for instability, which may be problem-dependent, is related to the underlying integrator and not an aspect of the multiple-material model. The precise threshold for this instability and its root cause remain topics for further investigation. When Newton's method is used, we imposed an absolute $L_1$ convergence tolerance of at least $10^{-10}$ in the nondimensional test cases and $10^{-7}$ in the dimensional water-air shock tube problem of Section 5.5. For the results presented here, we assign the single mixed-cell pressure as the spatially averaged value of the two sub-cell pressures of the constituent materials, i.e., as that given in Eq. (4.23). We present graphical results consisting of snapshots of the computed and exact flow fields at the final time along with time-histories of the material state properties of the two materials in the multi-material cell or, in the pure-material calculation, adjacent to the interface. Additionally, we quantify the error between the computed results and the exact solution.
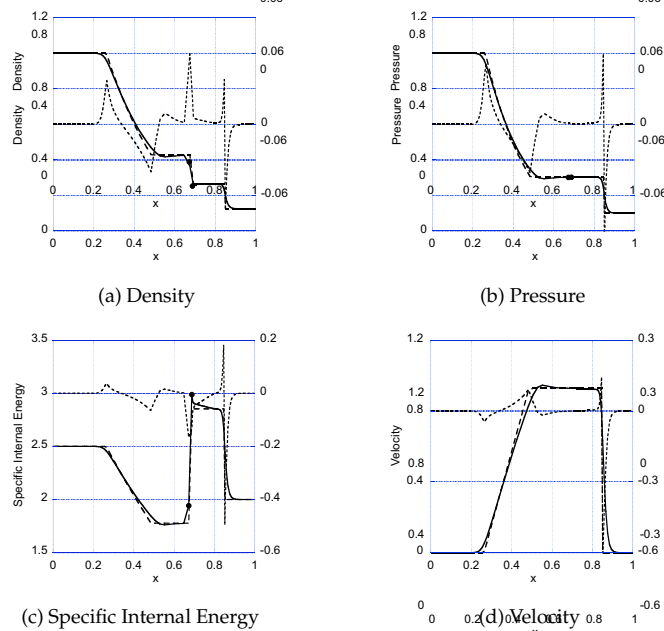
(a) Density

(b) Pressure

(c) Specific Internal Energy

(d) Velocity

Figure 3: Computed results (solid line) for the Sod shock tube problem with the new method for 99 zones on [0,1] at $t=0.2$. The difference (dotted line) between the computed and exact (dashed line) solutions is plotted against the right ordinate. The values corresponding to the individual materials in the mixed cell are denoted by the symbol •.

## 5.1  The Sod shock tube

The Sod shock tube problem [29] is defined as the behavior of a polytropic gas with the following non-dimensional initial conditions:

$$(\gamma,\rho,\varepsilon,p,u)=\begin{cases}(1.4,\,1,\qquad 2.5,\,1,\quad 0), & \text{if } 0\ <x<0.5,\\(1.4,\,0.125,\,2,\quad 0.1,\,0), & \text{if } 0.5<x<1,\end{cases}\qquad(5.1)$$

with a final time of $t_{final}=0.2$. This single-material problem is run to verify our basic implementation of the two-material algorithms. We refer to the material to the left of $x=0.5$ ("the interface") as "material 1" and the material to the right as "material 2." The initial condition of the mixed cell, centered at $x=0.5$, consists of these two disparate states. The developing structure consists of a rarefaction wave moving to the left, a contact discontinuity (corresponding to the initial discontinuity between the two states) moving right, and a shockwave moving right (faster than the contact). The exact solution to this problem is evaluated and used to quantify the error in the computed solution.

Results of our method on this problem are shown in Figs. 3-10. Shown in Fig. 3 are, clockwise from the upper left, plots of the mass density, pressure, velocity, and SIE at the final time. These plots contain the computed values (solid line) and exact solution (dashed line) plotted against the left ordinate and the signed difference between the exact and computed results (dotted line) plotted against the right ordinate. The values

(a) Density

(b) Pressure
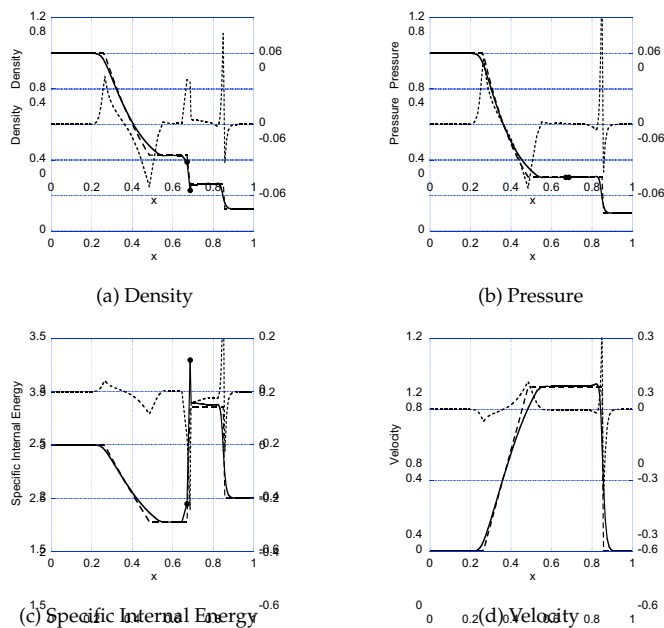
(c) Specific Internal Energy

(d) Velocity

Figure 4: Computed results (solid line) for the Sod shock tube problem with Tipton's method for 99 zones on $[0,1]$ at $t=0.2$. The difference (dotted line) between the computed and exact (dashed line) solutions is plotted against the right ordinate. The values corresponding to the individual materials in the mixed cell are denoted by the symbol ●.



(a) Density

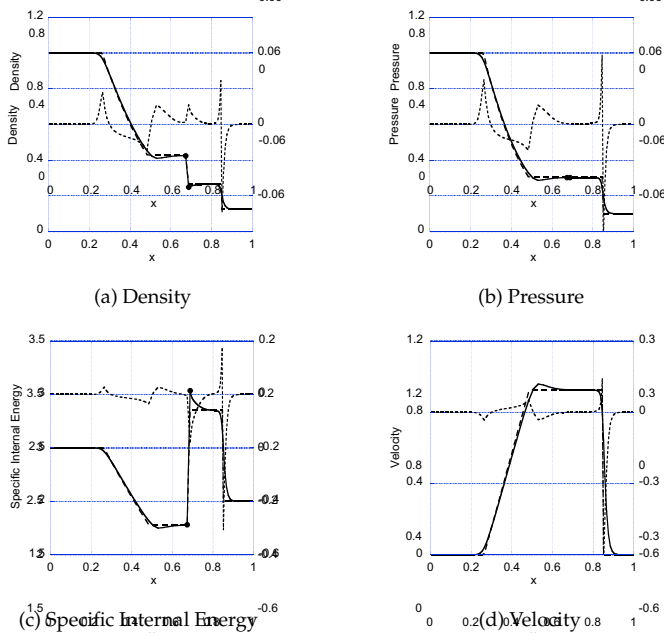(b) Pressure

(c) Specific Internal Energy

(d) Velocity

Figure 5: Computed results (solid line) for the Sod shock tube problem with pure cells for 100 zones on $[0,1]$ at $t=0.2$. The difference (dotted line) between the computed and exact (dashed line) solutions is plotted against the right ordinate. The values for the individual materials adjacent to the interface are denoted by the symbol ●.
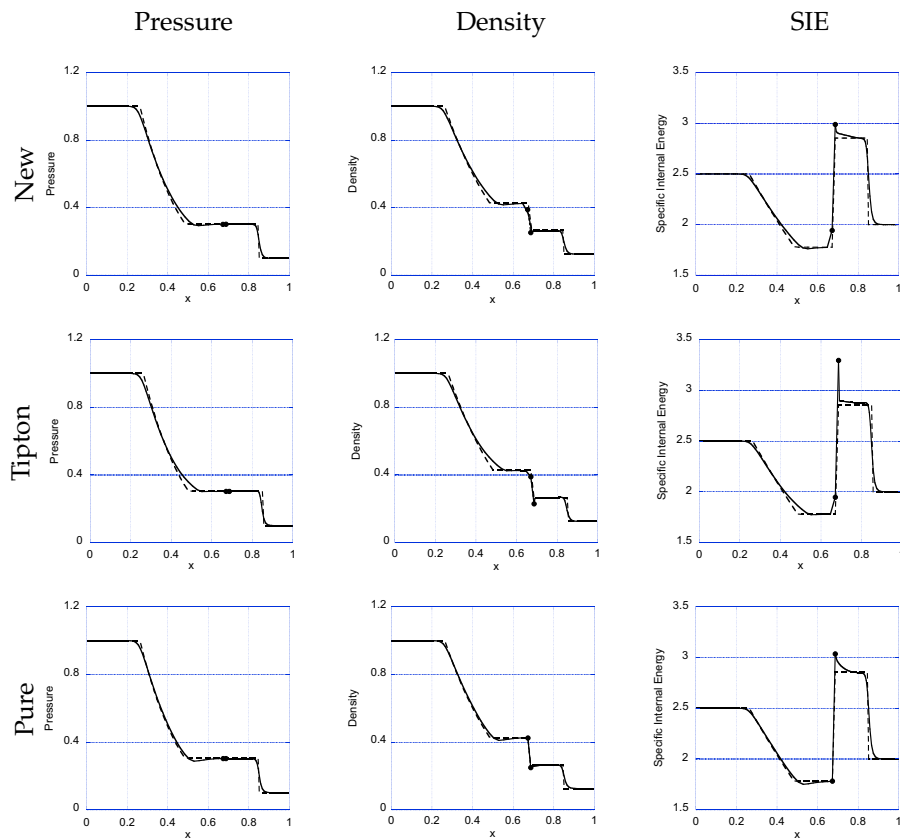
Figure 6: Results for the Sod shock tube problem on $[0,1]$ at $t=0.2$ for (from left to right) pressure, mass density, and SIE, with (from top to bottom) the new method (99 zones), Tipton's method (99 zones), and the pure-cell calculation (100 zones). The computed results are the solid line and the exact solution is the dashed line.
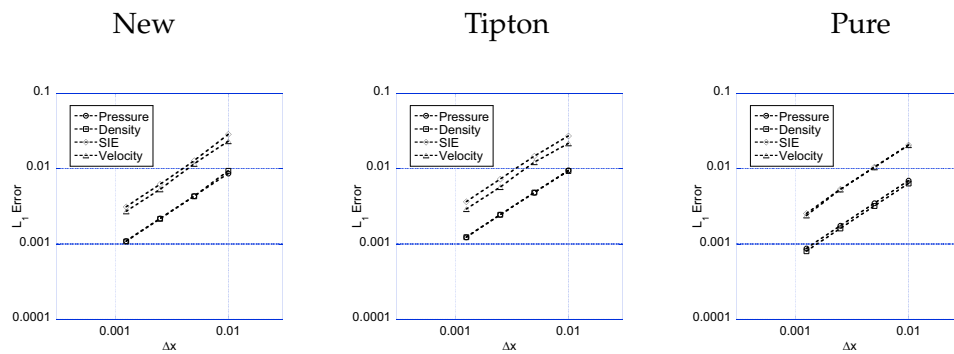


Figure 7: Plot of the $L_1$ norm of the difference between the computed results and exact solution on $[0,1]$ at $t=0.2$ for the Sod shock tube problem with the new method (left), Tipton's method (center) and the pure-material calculations (right). The values of the norm for the 99-, 199-, 399-, and 799-zone multi-material calculations and the 100-, 200-, 400- and 800-cell pure-material calculation are shown for the pressure ($\circ$), density ($\square$), SIE ($\diamond$), and velocity ($\triangle$). The curve fit parameters corresponding to these data are given in Table 1.

Table 1: $L_1$ norms of the difference between exact and computed Sod problem results, computed pointwise at $t=0.2$, for the given variables with the indicated number of points on the unit interval for, from top to bottom, the new method, Tipton's method, and the pure-material calculation. The prefactor $\mathcal{A}$ and convergence rate $\sigma$ are least-squares fits to the relation given in Eq. (5.2). The values of $\sigma$ close to unity suggest first-order convergence.

| | New Method | | | | | |
|---|---|---|---|---|---|---|
| | 99 | 199 | 399 | 799 | $\mathcal{A}$ | $\sigma$ |
| $p$ | $8.62 \times 10^{-3}$ | $4.32 \times 10^{-3}$ | $2.19 \times 10^{-3}$ | $1.09 \times 10^{-3}$ | 0.83 | 0.99 |
| $\rho$ | $8.56 \times 10^{-3}$ | $4.30 \times 10^{-3}$ | $2.16 \times 10^{-3}$ | $1.09 \times 10^{-3}$ | 0.83 | 0.99 |
| $e$ | $2.48 \times 10^{-2}$ | $1.27 \times 10^{-2}$ | $6.21 \times 10^{-3}$ | $3.12 \times 10^{-3}$ | 2.52 | 1.00 |
| $u$ | $2.30 \times 10^{-2}$ | $1.16 \times 10^{-2}$ | $5.32 \times 10^{-3}$ | $2.71 \times 10^{-3}$ | 2.75 | 1.04 |

| | Tipton's Method | | | | | |
|---|---|---|---|---|---|---|
| | 99 | 199 | 399 | 799 | $\mathcal{A}$ | $\sigma$ |
| $p$ | $9.46 \times 10^{-3}$ | $4.78 \times 10^{-3}$ | $2.44 \times 10^{-3}$ | $1.23 \times 10^{-3}$ | 0.83 | 0.97 |
| $\rho$ | $9.28 \times 10^{-3}$ | $4.82 \times 10^{-3}$ | $2.45 \times 10^{-3}$ | $1.23 \times 10^{-3}$ | 0.87 | 0.98 |
| $e$ | $2.70 \times 10^{-2}$ | $1.46 \times 10^{-2}$ | $7.23 \times 10^{-3}$ | $3.63 \times 10^{-3}$ | 2.40 | 0.97 |
| $u$ | $2.16 \times 10^{-2}$ | $1.22 \times 10^{-2}$ | $5.67 \times 10^{-3}$ | $2.89 \times 10^{-3}$ | 2.04 | 0.98 |

| | Pure Material | | | | | |
|---|---|---|---|---|---|---|
| | 100 | 200 | 400 | 800 | $\mathcal{A}$ | $\sigma$ |
| $p$ | $6.33 \times 10^{-3}$ | $3.48 \times 10^{-3}$ | $1.75 \times 10^{-3}$ | $8.73 \times 10^{-4}$ | 0.68 | 1.00 |
| $\rho$ | $6.92 \times 10^{-3}$ | $3.19 \times 10^{-3}$ | $1.61 \times 10^{-3}$ | $8.01 \times 10^{-4}$ | 0.62 | 0.99 |
| $e$ | $2.05 \times 10^{-2}$ | $1.05 \times 10^{-2}$ | $5.32 \times 10^{-3}$ | $2.54 \times 10^{-3}$ | 2.11 | 1.00 |
| $u$ | $2.05 \times 10^{-2}$ | $1.04 \times 10^{-2}$ | $5.29 \times 10^{-3}$ | $2.39 \times 10^{-3}$ | 2.37 | 1.03 |

corresponding to the individual material in the mixed cell are indicated with the symbol •. Errors are present at the usual locations, e.g., at the head and tail of the rarefaction and at the shock, together with overshoots and undershoots at the contact. The SIE in Fig. 3(c) exhibits obvious overshoot on the rarefaction-side of the contact. Corresponding plots of results for the mixed-cell method of Tipton and the pure-cell calculation are given in Figs. 4 and 5. Comparison of the three methods' results (without the errors) for the mass density, pressure, and SIE is provided in Fig. (6), which shows that the results for all methods exhibit slight differences: the tail of the rarefaction is less accurate with Tipton's method, which also undershoots density and overshoots SIE at the contact most significantly. Table 1 catalogues the $L_1$ norm of the error between the computed results and the exact solution for the same flow variables, for each of the three methods on all meshes. Also included in that table is the outcome of fitting these results to the error ansatz,

$$||y_{\text{computed}} - y_{\text{exact}}||_1 = \mathcal{A}\, \Delta x^{\sigma}, \qquad (5.2)$$

where $\Delta x$ is the initial, uniform mesh spacing of the problem (in all but the mixed cell). These values are depicted graphically in Fig. 7. These results suggest overall first-order convergence of the methods in all cases.
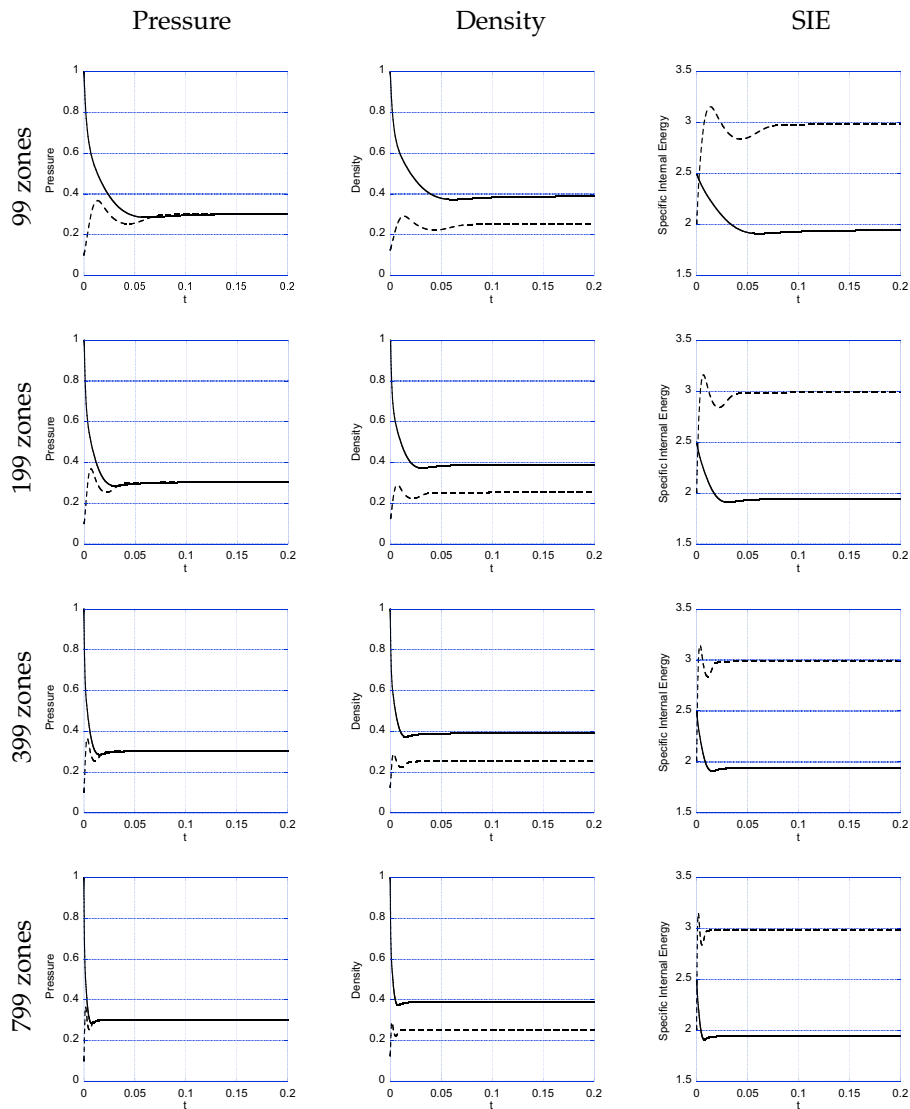
Figure 8: Time-history plots for the Sod shock tube problem on $[0,1]$ with the new method of the (from left to right) pressure, the mass density, and SIE of the two materials in the mixed cell, for the (from top to bottom) 99-, 199-, 399-, and 799-cell results. The solid line indicates the left material (material 1) and a dotted line represents the right material (material 2).

Fig. 8 contains time-history plots for the new method of the (from left to right) pressure, the mass density, and SIE of the two materials in the mixed cell, for the (from top to bottom) 99-, 199-, 399-, and 799-cell calculations. In these figures, the solid line indicates the left material (material 1) and a dotted line represents the right material (material 2). It is clear from these results that pressure equilibrium obtains for this problem by this method. Note that relaxation to pressure equilibrium is not monotonic in time. More-
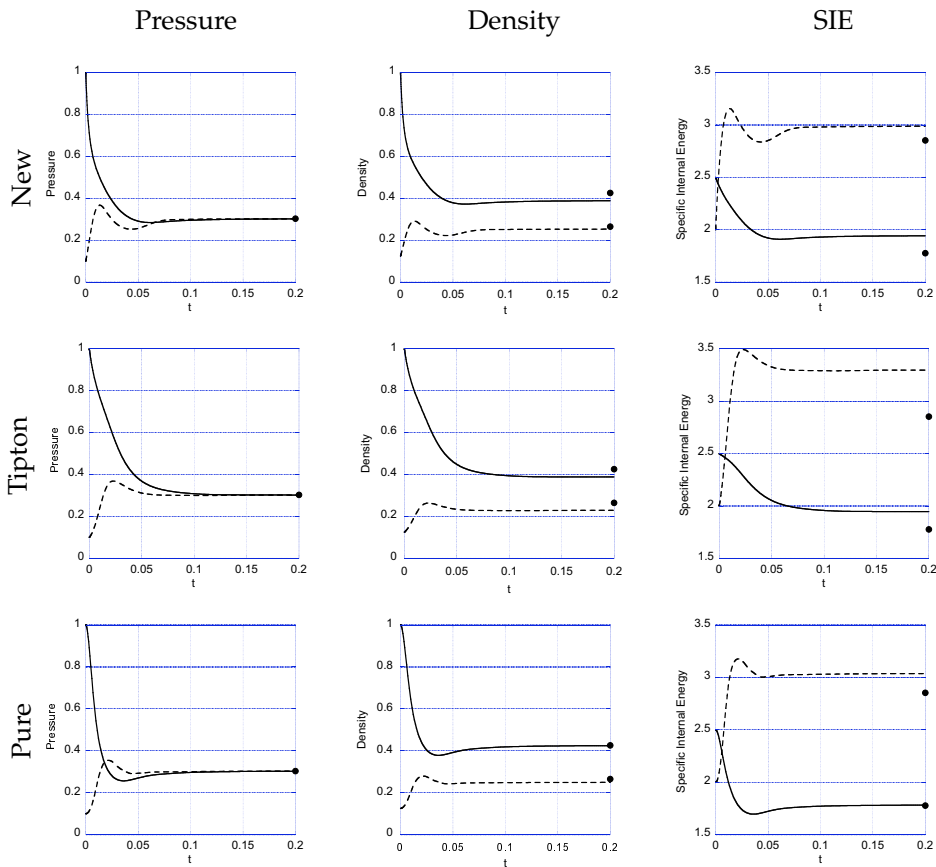
Figure 9: Time-history plots for the Sod shock tube problem on [0,1] of the (from left to right) pressure, the mass density, and SIE, with (from top to bottom) the new method (99 zones), Tipton's method (99 zones), and the pure-cell calculation (100 zones): the top two rows are for the two materials in the mixed cell, while the bottom row is for the cells immediately adjacent to the material interface. The solid line indicates the left material (material 1), the dotted line represents the right material (material 2), and the bullets represent the exact solution at the final time.

over, the zoning study shows that the effective relaxation effect is proportional to the mesh spacing; this characteristic is the same in all test problems considered and, so, we do not present the corresponding figures for the other problems. Fig. 9 contains plots of these time-histories on the coarsest grid for the three methods. The relaxation time is comparable for all methods, with Tipton's method perhaps slightly slower. The approach to equilibrium differs among the methods, however, with the final values of the new method closer to those of the pure-material calculation than to those of Tipton's method. Table 2 gives the values adjacent to the material interface at the final time on the finest grid, together with the exact solution at the contact interface. The Tipton locations and pressures are slightly closer to exact values, while the new method's locations and pressures are closer to the pure-material calculation; additionally, the density and SIE of
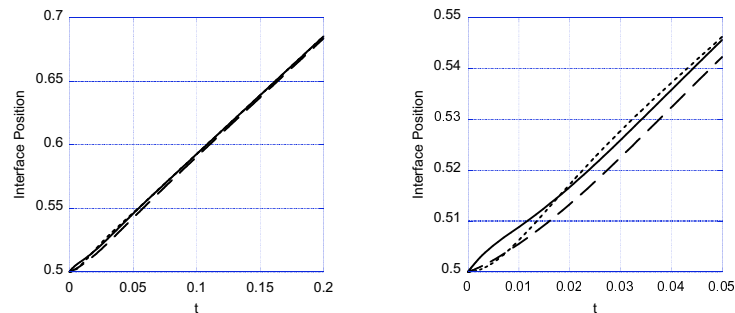
Figure 10: Plot of the position of the material interface as a function of time for the Sod shock tube problem on the coarsest mesh. The left plot shows the behavior for the entire simulation time, while the right plot shows the early-time behavior. The solid line corresponds to the new method, the dashed line to Tipton's method, and the dotted line to the pure-material calculation.

the new method are closer to both the exact and pure-material values. Fig. 10 shows the position of the material interface as a function of time. The methods' results vary slightly at early time (shown on the right), with the results of the new method very similar to those of the pure-material calculation at late time.

Table 2: Sod problem at $t=0.2$: the top two rows give the contact location for the exact solution and the material-centered positions adjacent to the interface for the computed results on the finest grid (new method in the mixed cell, Tipton's method in the mixed cell, and the pure-material calculation), while the subsequent rows contain the corresponding flow field values for the various approaches.

|         | Exact                    | New                      | Tipton                   | Pure                     |
|---------|--------------------------|--------------------------|--------------------------|--------------------------|
| $x_1$   | $6.85491 \times 10^{-1}$ | $6.83852 \times 10^{-1}$ | $6.83688 \times 10^{-1}$ | $6.83962 \times 10^{-1}$ |
| $x_2$   |                          | $6.85764 \times 10^{-1}$ | $6.85635 \times 10^{-1}$ | $6.85745 \times 10^{-1}$ |
| $p_1$   | $3.03130 \times 10^{-1}$ | $3.03123 \times 10^{-1}$ | $3.03128 \times 10^{-1}$ | $3.03119 \times 10^{-1}$ |
| $p_2$   | $3.03130 \times 10^{-1}$ | $3.03123 \times 10^{-1}$ | $3.03128 \times 10^{-1}$ | $3.03119 \times 10^{-1}$ |
| $\rho_1$ | $4.26319 \times 10^{-1}$ | $3.89645 \times 10^{-1}$ | $3.89070 \times 10^{-1}$ | $4.25102 \times 10^{-1}$ |
| $\rho_2$ | $2.65574 \times 10^{-1}$ | $2.53451 \times 10^{-1}$ | $2.29711 \times 10^{-1}$ | $2.49489 \times 10^{-1}$ |
| $e_1$   | 1.77760                  | 1.94487                  | 1.94777                  | 1.78263                  |
| $e_2$   | 2.85354                  | 2.98996                  | 3.29902                  | 3.03740                  |

## 5.2   The modified Sod shock tube

Various authors have proposed modifications to the standard Sod shock tube problem discussed in the previous section. We consider the variant introduced by Barlow [4] and described by Shashkov [28], with the following non-dimensional initial conditions:

$$(\gamma,\rho,\varepsilon,p,u) = \begin{cases} (2, \quad 1, \quad \ 2, 2, \quad 0), & \text{if } 0 < x < 0.5, \\ (1.4, 0.125, 2, 0.1, 0), & \text{if } 0.5 < x < 1, \end{cases} \tag{5.3}$$

(a) Density

(b) Pressure
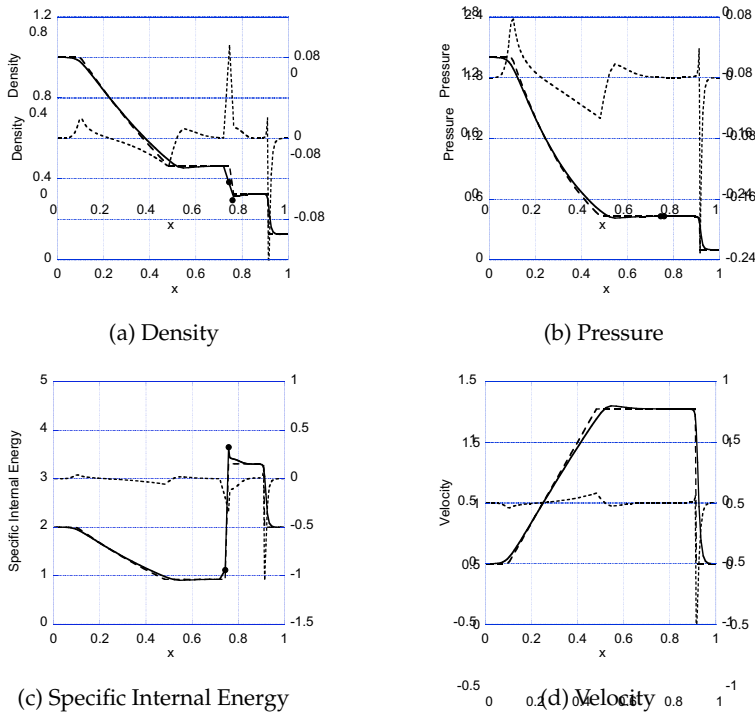
(c) Specific Internal Energy

(d) Velocity

Figure 11: Computed results (solid line) for the modified Sod shock tube problem with the new method for 99 zones on $[0,1]$ at $t=0.2$. The difference (dotted line) between the computed and exact (dashed line) solutions is plotted against the right ordinate. The values corresponding to the individual materials in the mixed cell are denoted by the symbol ●.

with a final time of $t_{final}=0.2$. As for the standard Sod case, the initial condition of the mixed cell, again centered at $x=0.5$, contains both of these two distinct states; unlike the that case, however, this is a genuine two-material problem. The solution structure is the same as the standard Sod case; however, this modified problem allows one to test the truly multi-material aspects of our algorithm.

Results of our method on this problem are shown in Figs. 11-15. Shown in Fig. 11 are, clockwise from the upper left, plots of the mass density, pressure, velocity, and SIE at the final time. These plots contain the computed values (solid line) and exact solution (dashed line) plotted against the left ordinate and the signed difference between the exact and computed results (dotted line) plotted against the right ordinate. The values corresponding to the individual material in the mixed cell are indicated with the symbol ●. The stronger initial pressure difference of this problem leads to greater over- and undershoot at the shock than the standard Sod problem; as in the standard Sod results, overshoot in the rarefaction-side SIE is seen. Fig. 12 contains results for all three methods. The results are similar to those for the standard Sod problem, with the Tipton method results standing out by having the least accurate rarefaction tail as well as the greatest density undershoot and SIE overshoot at the contact.
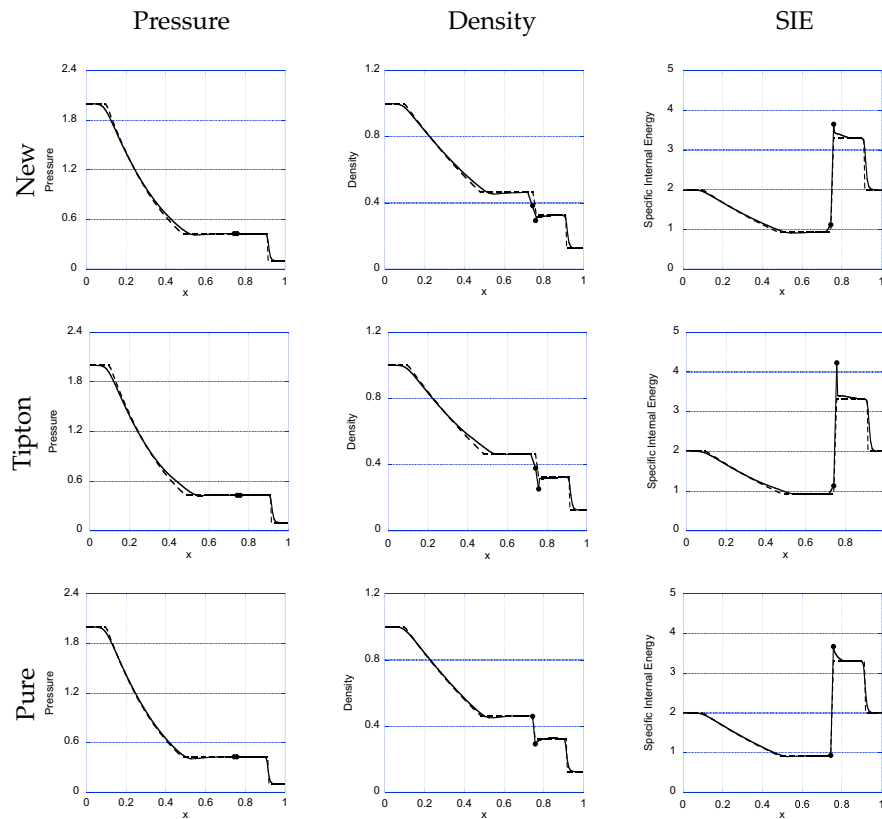
Figure 12: Results for the modified Sod shock tube problem on $[0,1]$ at $t=0.2$ for (from left to right) pressure, mass density, and SIE, with (from top to bottom) the new method (99 zones), Tipton's method (99 zones), and the pure-cell calculation (100 zones). The computed results are the solid line and the exact solution is the dashed line.
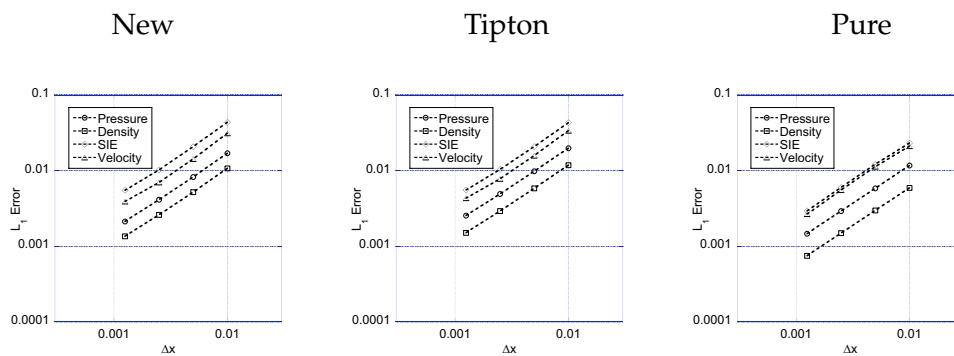


Figure 13: Plot of the $L_1$ norm of the difference between the computed results and exact solution on $[0,1]$ at $t=0.2$ for the modified Sod shock tube problem with the new method (left), Tipton's method (center) and the pure-material calculations (right). The values of the norm for the 99-, 199-, 399-, and 799-zone multi-material calculations and the 100-, 200-, 400- and 800-cell pure-material calculation are shown for the pressure ($\circ$), density ($\square$), SIE ($\diamond$), and velocity ($\triangle$). The curve fit parameters corresponding to these data are given in Table 3.

Table 3: $L_1$ norms of the difference between exact and computed modified Sod problem results, computed pointwise at $t = 0.2$, for the given variables with the indicated number of points on the unit interval for, from top to bottom, the new method, Tipton's method, and the pure-material calculation. The prefactor $\mathcal{A}$ and convergence rate $\sigma$ are least-squares fits to the relation given in Eq. (5.2). The values of $\sigma$ close to unity suggest first-order convergence.

| | New Method | | | | | |
|---|---|---|---|---|---|---|
| | 99 | 199 | 399 | 799 | $\mathcal{A}$ | $\sigma$ |
| $p$ | $1.70 \times 10^{-2}$ | $8.23 \times 10^{-3}$ | $4.12 \times 10^{-3}$ | $2.13 \times 10^{-3}$ | 1.66 | 1.00 |
| $\rho$ | $1.07 \times 10^{-2}$ | $5.22 \times 10^{-3}$ | $2.61 \times 10^{-3}$ | $1.35 \times 10^{-3}$ | 1.04 | 1.00 |
| $e$ | $4.37 \times 10^{-2}$ | $3.07 \times 10^{-2}$ | $1.03 \times 10^{-2}$ | $5.49 \times 10^{-3}$ | 4.22 | 1.00 |
| $u$ | $3.12 \times 10^{-2}$ | $1.42 \times 10^{-2}$ | $7.00 \times 10^{-3}$ | $3.91 \times 10^{-3}$ | 2.99 | 1.00 |

| | Tipton's Method | | | | | |
|---|---|---|---|---|---|---|
| | 99 | 199 | 399 | 799 | $\mathcal{A}$ | $\sigma$ |
| $p$ | $1.98 \times 10^{-2}$ | $9.82 \times 10^{-3}$ | $4.93 \times 10^{-3}$ | $2.54 \times 10^{-3}$ | 1.86 | 0.99 |
| $\rho$ | $1.18 \times 10^{-2}$ | $5.82 \times 10^{-3}$ | $2.92 \times 10^{-3}$ | $1.51 \times 10^{-3}$ | 1.11 | 0.99 |
| $e$ | $4.31 \times 10^{-2}$ | $2.09 \times 10^{-2}$ | $1.04 \times 10^{-2}$ | $5.56 \times 10^{-3}$ | 3.98 | 0.99 |
| $u$ | $3.37 \times 10^{-2}$ | $1.58 \times 10^{-2}$ | $7.80 \times 10^{-3}$ | $4.32 \times 10^{-3}$ | 3.11 | 0.99 |

| | Pure Material | | | | | |
|---|---|---|---|---|---|---|
| | 100 | 200 | 400 | 800 | $\mathcal{A}$ | $\sigma$ |
| $p$ | $1.17 \times 10^{-2}$ | $5.84 \times 10^{-3}$ | $2.93 \times 10^{-3}$ | $1.47 \times 10^{-3}$ | 1.15 | 1.00 |
| $\rho$ | $5.92 \times 10^{-3}$ | $2.98 \times 10^{-3}$ | $1.50 \times 10^{-3}$ | $7.49 \times 10^{-4}$ | 0.58 | 0.99 |
| $e$ | $2.33 \times 10^{-2}$ | $1.21 \times 10^{-2}$ | $6.01 \times 10^{-3}$ | $2.95 \times 10^{-3}$ | 2.32 | 1.00 |
| $u$ | $2.11 \times 10^{-2}$ | $1.13 \times 10^{-2}$ | $5.55 \times 10^{-3}$ | $2.67 \times 10^{-3}$ | 2.15 | 1.00 |

Table 3 shows the $L_1$ norm of the error between the computed results and the exact solution for these flow variables, for each of the three methods on all meshes, together with the fit of those results to the ansatz in Eq. (5.2). The convergence results are slightly more uniform for this problem than for the standard Sod problem. These values are plotted in Fig. 13.

Plots of time-histories on the coarsest grid for all three methods are shown in Fig. 14. The nature of the pressure-equilibration varies among the three methods. The final values of density and SIE differ slightly among methods, with those of the new and pure-material calculation being more similar to each other than to the Tipton values. The time-history results under mesh resolution are qualitatively very similar to those of the standard Sod problem.

Table 4 gives the values adjacent to the material interface at the final time on the finest grid, together with the exact solution at the contact interface. The results for the new method are, in general, closer to the corresponding values for both the exact and pure-material calculations. Fig. 15 shows the position of the material interface as a function of time. These results are similar to the standard Sod problem results, with the results of the new method similar to those of the pure-material calculation at all but the earliest times.
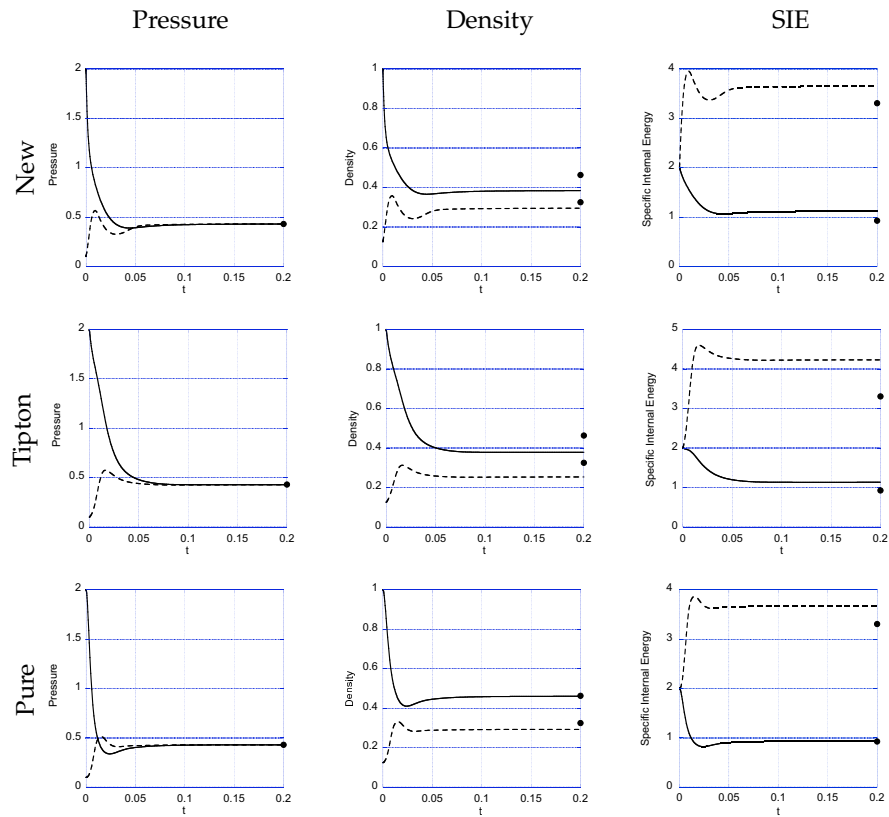
Figure 14: Time-history plots for the modified Sod shock tube problem of the (from left to right) pressure, the mass density, and SIE, with (from top to bottom) the new method (99 zones), Tipton's method (99 zones), and the pure-cell calculation (100 zones): the top two rows are for the two materials in the mixed cell, while the bottom row is for the cells immediately adjacent to the material interface. The solid line indicates the left material (material 1), the dotted line represents the right material (material 2), and the bullets represent the exact solution at the final time.
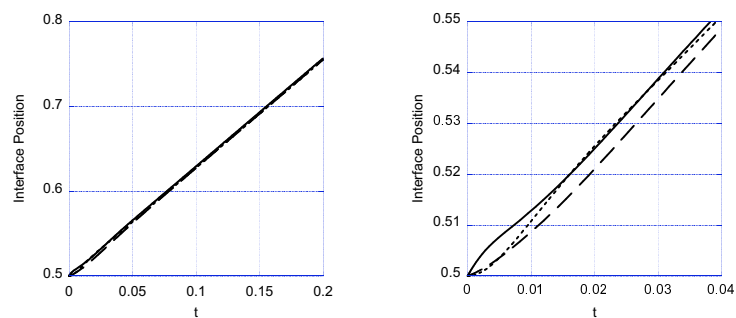


Figure 15: Plot of the position of the material interface as a function of time for the modified Sod shock tube problem on the coarsest mesh. The left plot shows the behavior for the entire simulation time, while the right plot shows the early-time behavior. The solid line corresponds to the new method, the dashed line to Tipton's method, and the dotted line to the pure-material calculation.

Table 4: Modified Sod problem at $t=0.2$: the top two rows give the contact location for the exact solution and the material-centered positions adjacent to the interface for the computed results on the finest grid (new method in the mixed cell, Tipton's method in the mixed cell, and the pure-material calculation), while the subsequent rows contain the corresponding flow field values for the various approaches.

|  | Exact | New | Tipton | Pure |
|---|---|---|---|---|
| $x_1$ | $7.55142 \times 10^{-1}$ | $7.53723 \times 10^{-1}$ | $7.53528 \times 10^{-1}$ | $7.53760 \times 10^{-1}$ |
| $x_2$ |  | $7.55615 \times 10^{-1}$ | $7.55485 \times 10^{-1}$ | $7.55384 \times 10^{-1}$ |
| $p_1$ | $4.30332 \times 10^{-1}$ | $4.30325 \times 10^{-1}$ | $4.30329 \times 10^{-1}$ | $4.30323 \times 10^{-1}$ |
| $p_2$ | $4.30332 \times 10^{-1}$ | $4.30325 \times 10^{-1}$ | $4.30329 \times 10^{-1}$ | $4.30323 \times 10^{-1}$ |
| $\rho_1$ | $4.63860 \times 10^{-1}$ | $3.84173 \times 10^{-1}$ | $3.79078 \times 10^{-1}$ | $4.60497 \times 10^{-1}$ |
| $\rho_2$ | $3.25380 \times 10^{-1}$ | $2.94700 \times 10^{-1}$ | $2.54108 \times 10^{-1}$ | $2.92835 \times 10^{-1}$ |
| $e_1$ | $9.27720 \times 10^{-1}$ | $1.12013$ | $1.13520$ | $9.34476 \times 10^{-1}$ |
| $e_2$ | $3.30638$ | $3.65053$ | $4.23372$ | $3.67377$ |

## 5.3 Moving shock problem

Like the first Sod problem, the moving shock problem is a single-material test, but of a fundamentally different phenomenon. This problem tests the steady propagation of a shock wave in a uniform material and is used to assesses the impact of the multi-material algorithm on the otherwise uniform flow. The non-dimensional initial conditions are:

$$(\gamma, \rho, \varepsilon, p, u) = \begin{cases} (5/3, 4, \ 0.5, \ 4/3, \ 1), & \text{if } -1 < x < 0, \\ (5/3, 1, \ 10^{-4}, \ 2/3 \times 10^{-4}, 0), & \text{if } 0 < x < 1, \end{cases} \quad (5.4)$$

with a final time of $t_{final}=0.5$. These initial conditions approximate an infinitely strong shock wave moving into quiescent gas at speed $u_s=4/3$. The default mesh for this problem contains 255 cells on $-1 \le x \le 1$. The mixed cell is initially centered at $x=0.0$ and contains the two states indicated above.

Results of our method on this problem are shown in Figs. 16-20. Shown in Fig. 16 are, clockwise from the upper left, plots of the mass density, pressure, velocity, and SIE at the final time; again, the computed values (solid line) and exact solution (dashed line) are plotted against the left ordinate and the signed differences between these values (dotted line) are plotted against the right ordinate, with the mixed-cell values indicated by the symbol •. The perturbation in the results to the right of the origin in these plots is a residual of the start-up error associated with the initial shock location at the origin.[**] The additional discrepancies in the solutions are associated with the original interface (at $x=0.5$) and the shock (at $x=2/3$), where, again, over- and under-shoots occur, with the density overshoot being most pronounced. Comparison of coarse-grid results for these quantities in Fig. 17 indicates that both the new method and Tipton's method produce the most significant discrepancies near the contact in mass density and SIE. Table 5 shows the $L_1$ norm of the error between the computed results and the exact solution for these flow

---

[**]Evocative of this phenomenon are post-shock oscillations, as discussed by Arora & Roe [2] and LeVeque [20] for Eulerian shock capturing schemes.

(a) Density

(b) Pressure
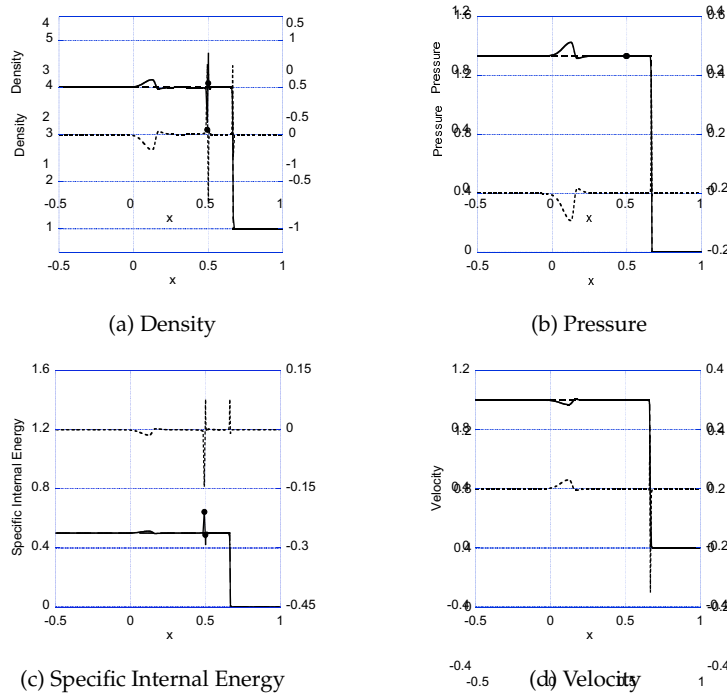
(c) Specific Internal Energy

(d) Velocity

Figure 16: Computed results (solid line) for the moving shock with the new method for 255 zones on $[-1,1]$ at $t = 0.5$. The difference (dotted line) between the computed and exact (dashed line) solutions is plotted against the right ordinate. The values corresponding to the individual materials in the mixed cell are denoted by the symbol •.

variables, for each of the three methods on all meshes, together with the fit of those results to the ansatz in Eq. (5.2). These values are depicted graphically in Fig. 18. These results again suggest overall first-order convergence of the methods.

Time-histories on the coarsest grid for the three methods are given in Fig. 19. The results for the new method here present a clear example of the pressure difference decreasing at early time, increasing at intermediate time, and then relaxing to zero at late times. The pressure histories for this problem support the contention posited in Section 4.2, that the pressures computed with this model do relax to equilibrium, but in a possibly non-monotonic manner. Comparison of these calculations shows notable differences in behavior. While the pressure for each method equilibrates to approximately the same value, the time-dependence of that relaxation clearly differs among the methods. The mass density and SIE show notably different behavior: the new method and pure-material calculation give final values that are more similar than the Tipton values, which are of reversed order. Table 6 gives the values adjacent to the material interface at the final time on the finest grid, together with the exact solution at the contact interface. For both Tipton and the pure-material calculation, the interface is slightly to the left of (behind) where it should be; however, the new method gives slightly greater (resp., smaller) point-wise error in material 1 (resp., 2) than Tipton and the pure-material result. Fig. 20
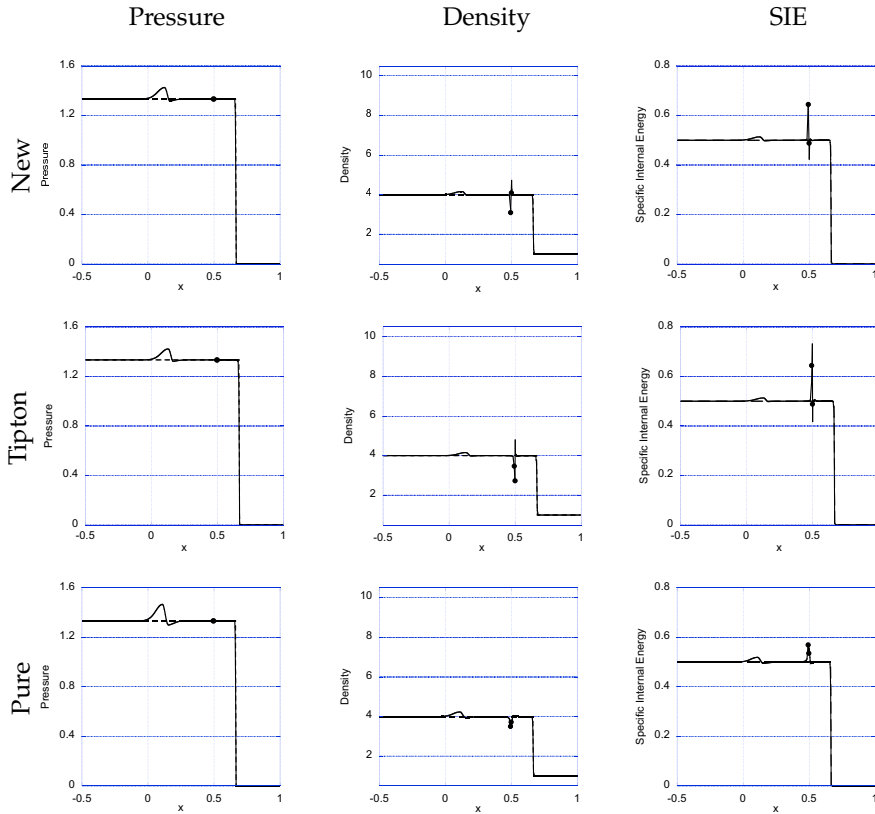
Figure 17: Results for the moving shock problem on $[-1,1]$ at $t=0.5$ with (from left to right) the new method (255 zones), Tipton's method (255 zones), and the pure-cell calculation (256 zones), for (from top to bottom) density, pressure, SIE, and velocity. The computed results are the solid line and the exact solution is the dashed line.
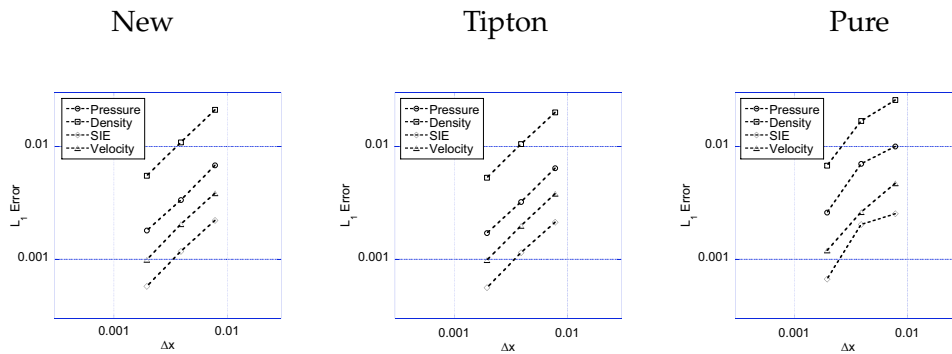


Figure 18: Plot of the $L_1$ norm of the difference between the computed results and exact solution for the moving shock problem on $[-1,1]$ at $t=0.5$ with the new method (left), Tipton's method (center) and the pure-material calculations (right). The values of the norm for the 255-, 511-, and 1023-zone multi-material calculations and the 256-, 512-, and 1024-cell pure-material calculation are shown for the pressure ($\circ$), density ($\square$), SIE ($\diamond$), and velocity ($\triangle$). The curve fit parameters corresponding to these data are given in Table 5.

Table 5: $L_1$ norms of the difference between exact and computed moving shock problem results, computed pointwise at $t = 0.5$, for the given variables with the indicated number of points on the unit interval for, from top to bottom, the new method, Tipton's method, and the pure-material calculation. The prefactor $\mathcal{A}$ and convergence rate $\sigma$ are least-squares fits to the relation given in Eq. (5.2). The values of $\sigma$ close to unity suggest first-order convergence.

| | New Method | | | | |
|---|---|---|---|---|---|
| | 255 | 511 | 1023 | $\mathcal{A}$ | $\sigma$ |
| $p$ | $6.77 \times 10^{-3}$ | $3.34 \times 10^{-3}$ | $1.80 \times 10^{-3}$ | 0.69 | 0.96 |
| $\rho$ | $2.12 \times 10^{-2}$ | $1.09 \times 10^{-2}$ | $5.55 \times 10^{-3}$ | 2.30 | 0.97 |
| $e$ | $2.29 \times 10^{-3}$ | $1.22 \times 10^{-3}$ | $5.98 \times 10^{-4}$ | 0.25 | 0.97 |
| $u$ | $3.83 \times 10^{-3}$ | $2.05 \times 10^{-3}$ | $9.89 \times 10^{-4}$ | 0.45 | 0.98 |

| | Tipton's Method | | | | |
|---|---|---|---|---|---|
| | 255 | 511 | 1023 | $\mathcal{A}$ | $\sigma$ |
| $p$ | $6.39 \times 10^{-3}$ | $3.21 \times 10^{-3}$ | $1.70 \times 10^{-3}$ | 0.65 | 0.96 |
| $\rho$ | $1.98 \times 10^{-2}$ | $1.04 \times 10^{-2}$ | $5.26 \times 10^{-3}$ | 2.09 | 0.95 |
| $e$ | $2.13 \times 10^{-3}$ | $1.15 \times 10^{-3}$ | $5.61 \times 10^{-4}$ | 0.23 | 0.96 |
| $u$ | $3.80 \times 10^{-3}$ | $1.98 \times 10^{-3}$ | $9.84 \times 10^{-4}$ | 0.43 | 0.97 |

| | Pure Material | | | | |
|---|---|---|---|---|---|
| | 256 | 512 | 1024 | $\mathcal{A}$ | $\sigma$ |
| $p$ | $9.93 \times 10^{-3}$ | $6.99 \times 10^{-3}$ | $2.59 \times 10^{-3}$ | 1.22 | 0.97 |
| $\rho$ | $2.56 \times 10^{-2}$ | $1.67 \times 10^{-2}$ | $6.73 \times 10^{-3}$ | 2.98 | 0.96 |
| $e$ | $2.53 \times 10^{-3}$ | $2.03 \times 10^{-3}$ | $6.69 \times 10^{-4}$ | 0.31 | 0.96 |
| $u$ | $4.70 \times 10^{-3}$ | $2.62 \times 10^{-3}$ | $1.20 \times 10^{-3}$ | 0.58 | 0.99 |

Table 6: Moving shock problem at $t = 0.5$: the top two rows give the contact location for the exact solution and the material-centered positions adjacent to the interface for the computed results on the finest grid (new method in the mixed cell, Tipton's method in the mixed cell, and the pure-material calculation), while the subsequent rows contain the corresponding flow field values for the various approaches.

| | Exact | New | Tipton | Pure |
|---|---|---|---|---|
| $x_1$ | $4.99987 \times 10^{-1}$ | $4.98560 \times 10^{-1}$ | $4.98419 \times 10^{-1}$ | $4.98302 \times 10^{-1}$ |
| $x_2$ | | $5.00058 \times 10^{-1}$ | $4.99900 \times 10^{-1}$ | $4.99676 \times 10^{-1}$ |
| $p_1$ | 1.33341 | 1.33338 | 1.33338 | 1.33336 |
| $p_2$ | 1.33341 | 1.33338 | 1.33338 | 1.33336 |
| $\rho_1$ | 4.00014 | 3.10224 | 3.47524 | 3.50964 |
| $\rho_2$ | 3.99925 | 4.09120 | 2.73574 | 3.73359 |
| $e_1$ | $5.00012 \times 10^{-1}$ | $6.44716 \times 10^{-1}$ | $5.75520 \times 10^{-1}$ | $5.69870 \times 10^{-1}$ |
| $e_2$ | $5.00123 \times 10^{-1}$ | $4.88870 \times 10^{-1}$ | $7.31090 \times 10^{-1}$ | $5.35687 \times 10^{-1}$ |

shows the position of the material interface as a function of time. The methods' results differ slightly, even at early time (shown on the right): the pure-material calculation and Tipton's method have a similar time-history, with the interface slightly behind that of the new method at all times.
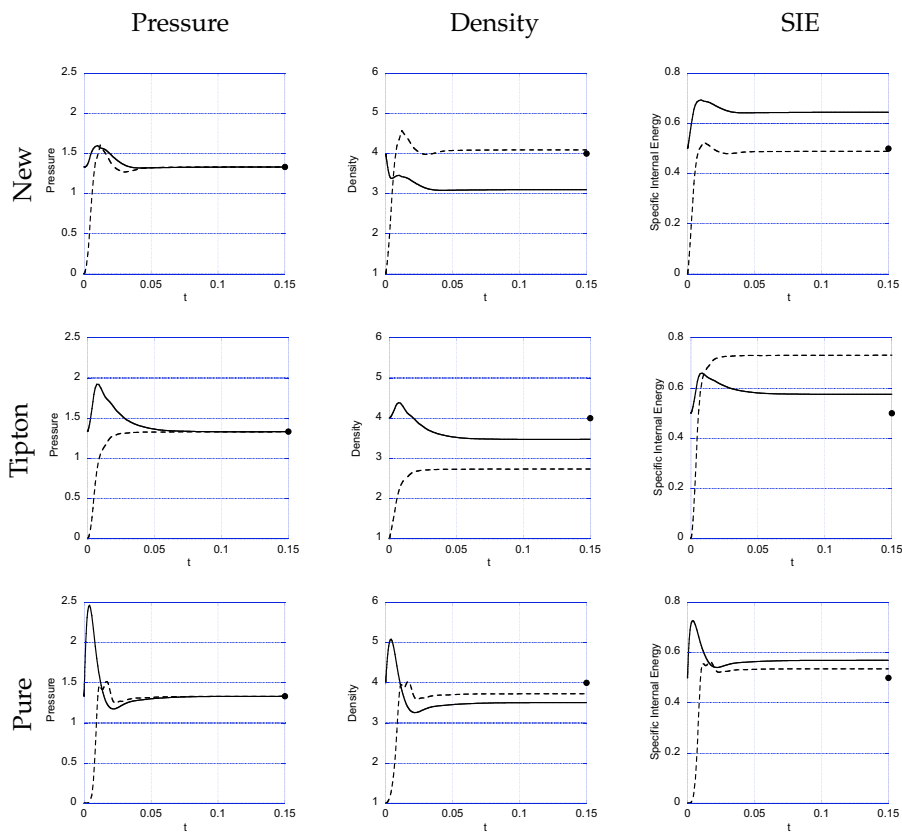
Figure 19: Time-history plots for the moving shock problem for (from left to right) pressure, mass density, and SIE with (from top to bottom) the new method (255 zones), Tipton's method (255 zones), and the pure-cell calculation (256 zones). The solid line indicates the left material (material 1), the dotted line represents the right material (material 2), and the bullets represent the exact solution at the final time.
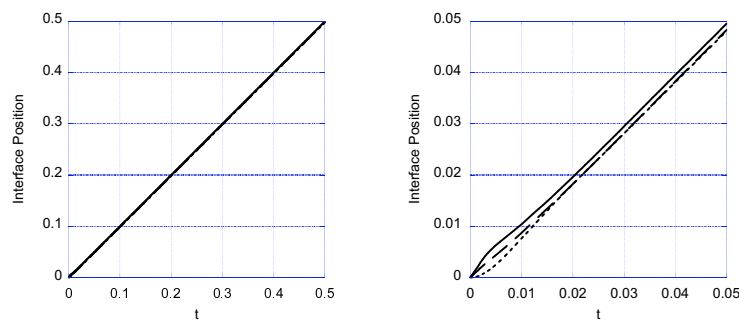


Figure 20: Plot of the position of the material interface as a function of time for the moving shock problem on the coarsest mesh. The left plot shows the behavior for the entire simulation time, while the right plot shows the early-time behavior. The solid line corresponds to the new method, the dashed line to Tipton's method, and the dotted line to the pure-material calculation.

Table 7: High-precision initial conditions for the shock-contact problem. This configuration corresponds to a Mach number of 2.0 and an initial shock speed of $u_S = 2.32379000772$, so that the shock hits the material interface at $t = 0.172132593165$.

|          | $0 < x < 0.1$   | $0.1 < x < 0.5$ | $0.5 < x < 1$   |
| -------- | --------------- | --------------- | --------------- |
| $\gamma$ | 1.35            | 1.35            | 5.0             |
| $p$      | 4.44680851064   | 1.0             | 1.0             |
| $\rho$   | 2.76470588235   | 1.0             | 1.9             |
| $e$      | 4.59548599884   | 2.85714285714   | 0.131578947368  |
| $u$      | 1.48327021770   | 0.0             | 0.0             |

Table 8: High-precision solution for the shock-contact problem at $t = 0.25$. Here, the reflected shock position is $x_{RS} = 0.472708981241754$, the contact position is $x_C = 0.572446778128859$, and the transmitted shock position is $x_{TS} = 0.775299530851478$. The speed of the reflected shock in the laboratory frame is $u_{RS} = -0.350480642253781$, and the speed of the transmitted shock is $u_{TS} = 3.53549118996649$.

|          | $0 < x < x_{RS}$ | $x_{RS} < x < x_C$ | $x_C < x < x_{TS}$ | $x_{TS} < x < 1$ |
| -------- | ---------------- | ------------------ | ------------------ | ---------------- |
| $\gamma$ | 1.35             | 1.35               | 5.0                | 5.0              |
| $p$      | 4.44680851064    | 7.24980870307      | 7.24980870307      | 1.0              |
| $\rho$   | 2.76470588235    | 3.95808583566      | 2.57856549437      | 1.9              |
| $e$      | 4.59548599884    | 5.23327184191      | 0.702891658064     | 0.131578947368   |
| $u$      | 1.48327021770    | 0.930386423194     | 0.930386423195     | 0.0              |

## 5.4  Shock-contact problem

This problem tests the transmission and reflection of a Mach 2 shock through an initially stationary contact discontinuity between two materials with disparate adiabatic indices. This problem was used by Banks et al. [3] to evaluate high-resolution Godunov algorithms for multi-material, compressible flow in the Eulerian frame. To three significant figures, the non-dimensional initial conditions are given by:

$$(\gamma, \rho, \varepsilon, p, u) = \begin{cases} (1.35, \ 2.76, \ 4.60, \ \ 4.45, \ 1.48), & \text{if } 0 < x < 0.1, \\ (1.35, \ 1.0, \ \ 2.86, \ \ 1.0, \ \ 0.0), & \text{if } 0.1 < x < 0.5, \\ (5.0, \ \ 1.9, \ \ 0.132, \ 1.0, \ \ 0.0), & \text{if } 0.5 < x < 1, \end{cases} \qquad (5.5)$$

with a final time of $t_{final} = 0.25$. The default mesh for this problem has 274 cells on the initial domain $-0.37 \leq x \leq 1$. In the calculations we use high-precision initial conditions, given in Table 7, corresponding to a Mach number of two with to a shock speed of $u_s \doteq 2.32$. The mixed cell is initially centered at $x = 0.5$ and contains the quiescent states of the materials with differing adiabatic indices. The shock meets this material interface at $t \doteq 0.172$. The numerical solution for the flow state at any time can be obtained using standard shock relations (see, e.g., the report by Hurricane & Miller [15]); high-precision results for the final time are given in Table 8.

   Results of our method on this problem are shown in Figs. 21-25. Shown in Fig. 21 are, clockwise from the upper left, plots of the computed (solid line) and exact (dashed
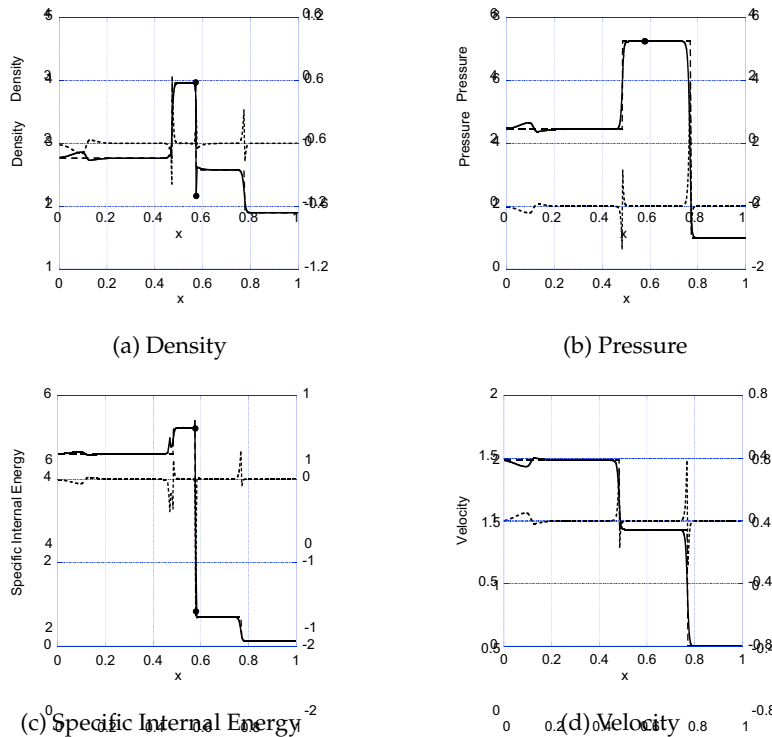
(a) Density

(b) Pressure

(c) Specific Internal Energy

(d) Velocity

Figure 21: Computed results (solid line) for the shock-contact problem with the new method at $t = 0.25$ for 274 zones initially on $[-0.37, 1]$. The difference (dotted line) between the computed and exact (dashed line) solutions is plotted against the right ordinate. The values corresponding to the individual materials in the mixed cell are denoted by the symbol $\bullet$.

line) mass density, pressure, velocity, and SIE at the final time, together with the signed difference between these values (dashed lines), as well as the mixed-cell values ($\bullet$). The residual of the start-up error is evident near the origin. The reflected shock is somewhat noisier in both density and SIE than the transmitted shock, while the contact exhibits a notable undershoot in the constituent density. Comparison of coarse-grid results for all methods in Fig. 22 shows that, near the contact in this problem, the new method has slightly greater undershoot in mass density than Tipton's method (the pure-material calculation has none). Also at the contact, the overshoot in SIE of Tipton's method is greater than either the new method or pure-material calculation. Table 9 catalogues the $L_1$ norm of the error between the computed results and the exact solution for these same flow variables, for each of the three methods on all meshes, together with the fit of those results to the ansatz in Eq. 5.2. These values are plotted in Fig. 23. These results again suggest approximately first-order convergence overall for this problem, although the convergence results for SIE are uniformly lower than for other quantities.

Fig. 24 contains time-histories on the coarsest grid for all three methods. For all methods, the approach to equilibrium is roughly similar; however, the pressure equilibration
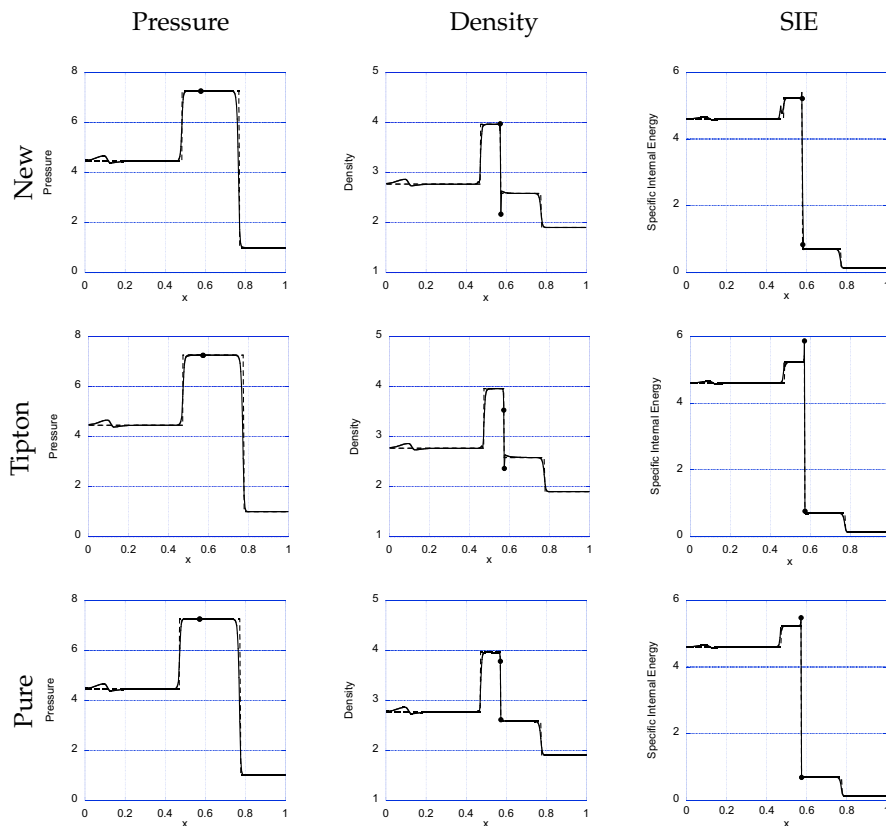
Figure 22: Results for the shock-contact problem at $t=0.25$ with (from left to right) the new method (274 zones), Tipton's method (274 zones), and the pure-cell calculation (275 zones), for (from top to bottom) density, pressure, SIE, and velocity. The computed results are the solid line and the exact solution is the dashed line.
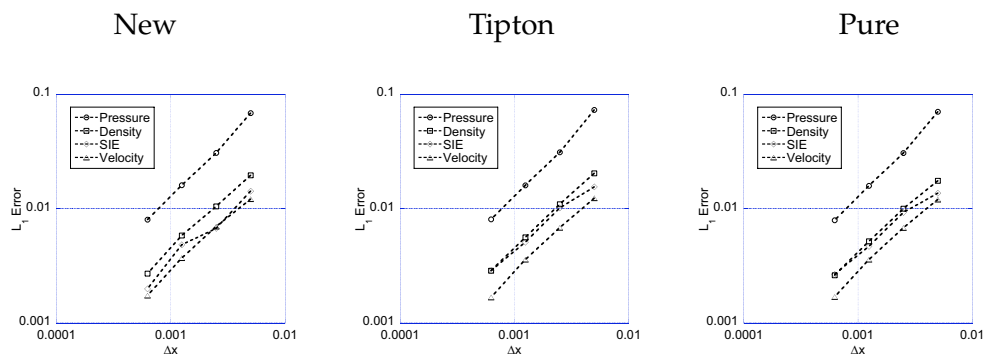


Figure 23: Plot of the $L_1$ norm of the difference between the computed results and exact solution at $t=0.25$ for the shock-contact problem with the new method (left), Tipton's method (center) and the pure-material calculations (right). The values of the norm for the 274-, 549-, 1099-, and 2199-zone multi-material calculations and the 275-, 550-, 1100-, and 2200-cell pure-material calculation are shown for the pressure ($\circ$), density ($\square$), SIE ($\diamond$), and velocity ($\triangle$). The curve fit parameters corresponding to these data are given in Table 9.
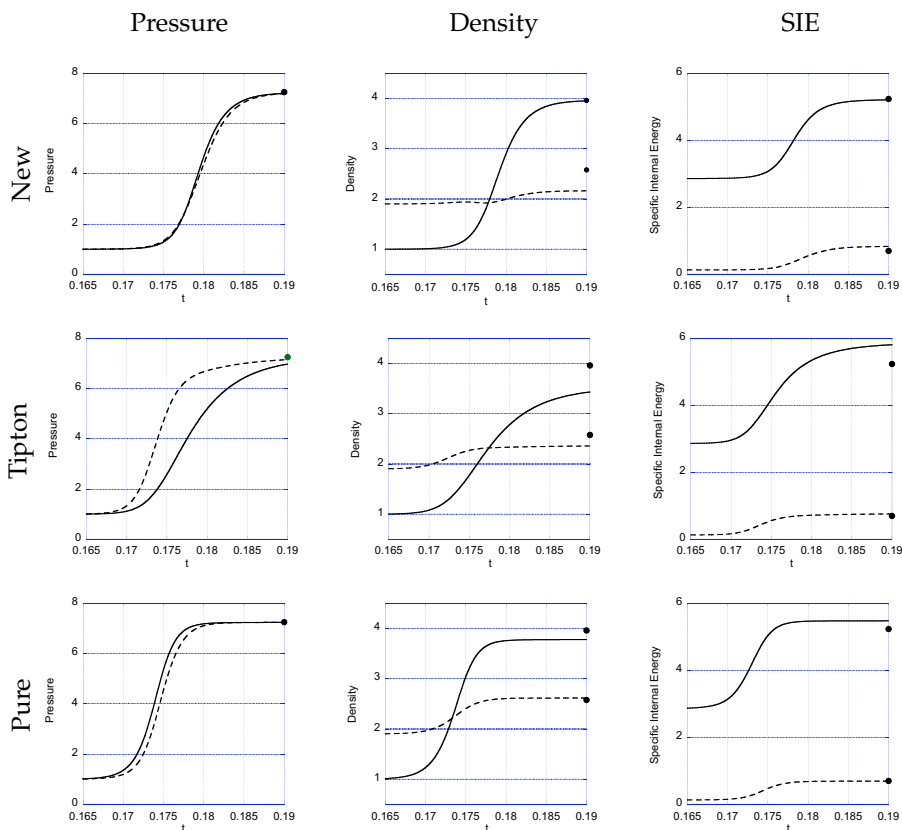
Figure 24: Close-up of time-history plots for the shock-contact problem for (from left to right) pressure, mass density, and SIE with (from top to bottom) the new method (274 zones), Tipton's method (274 zones), and the pure-cell calculation (275 zones). The solid line indicates the left material (material 1), the dotted line represents the right material (material 2), and the bullets represent the exact solution at the final time.
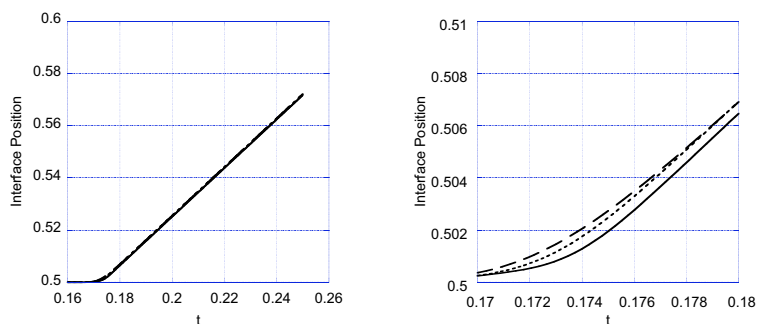


Figure 25: Plot of the position of the material interface as a function of time for the shock-contact problem on the coarsest mesh. The left plot shows the behavior for the entire simulation time, while the right plot shows the early-time behavior. The solid line corresponds to the new method, the dashed line to Tipton's method, and the dotted line to the pure-material calculation.

Table 9: $L_1$ norms of the difference between exact and computed shock-contact problem results, computed pointwise at $t = 0.25$, for the given variables with the indicated number of points on the unit interval for, from top to bottom, the new method, Tipton's method, and the pure-material calculation. The prefactor $\mathcal{A}$ and convergence rate $\sigma$ are least-squares fits to the relation given in Eq. (5.2). The values of $\sigma$ close to unity suggest first-order convergence.

| | New Method | | | | | |
| --- | --- | --- | --- | --- | --- | --- |
| | 274 | 549 | 1099 | 2199 | $\mathcal{A}$ | $\sigma$ |
| $p$ | $6.89 \times 10^{-2}$ | $3.09 \times 10^{-2}$ | $1.61 \times 10^{-2}$ | $8.05 \times 10^{-3}$ | 15.0 | 1.02 |
| $\rho$ | $1.97 \times 10^{-2}$ | $1.05 \times 10^{-2}$ | $5.85 \times 10^{-3}$ | $2.71 \times 10^{-3}$ | 2.97 | 0.94 |
| $e$ | $1.43 \times 10^{-2}$ | $6.76 \times 10^{-3}$ | $4.84 \times 10^{-3}$ | $1.99 \times 10^{-3}$ | 1.66 | 0.80 |
| $u$ | $1.22 \times 10^{-2}$ | $7.01 \times 10^{-3}$ | $3.71 \times 10^{-3}$ | $1.74 \times 10^{-3}$ | 1.79 | 0.93 |

| | Tipton's Method | | | | | |
| --- | --- | --- | --- | --- | --- | --- |
| | 274 | 549 | 1099 | 2199 | $\mathcal{A}$ | $\sigma$ |
| $p$ | $7.34 \times 10^{-2}$ | $3.13 \times 10^{-2}$ | $1.61 \times 10^{-2}$ | $8.09 \times 10^{-3}$ | 18.2 | 1.05 |
| $\rho$ | $2.04 \times 10^{-2}$ | $1.10 \times 10^{-2}$ | $5.64 \times 10^{-3}$ | $2.88 \times 10^{-3}$ | 3.09 | 0.94 |
| $e$ | $1.56 \times 10^{-2}$ | $1.02 \times 10^{-2}$ | $5.12 \times 10^{-3}$ | $2.87 \times 10^{-3}$ | 1.34 | 0.83 |
| $u$ | $1.24 \times 10^{-2}$ | $6.83 \times 10^{-3}$ | $3.60 \times 10^{-3}$ | $1.68 \times 10^{-3}$ | 2.06 | 0.96 |

| | Pure Material | | | | | |
| --- | --- | --- | --- | --- | --- | --- |
| | 275 | 550 | 1100 | 2200 | $\mathcal{A}$ | $\sigma$ |
| $p$ | $7.07 \times 10^{-2}$ | $3.08 \times 10^{-2}$ | $1.59 \times 10^{-2}$ | $7.94 \times 10^{-3}$ | 16.8 | 1.04 |
| $\rho$ | $1.76 \times 10^{-2}$ | $1.00 \times 10^{-2}$ | $5.20 \times 10^{-3}$ | $2.62 \times 10^{-3}$ | 2.38 | 0.92 |
| $e$ | $1.37 \times 10^{-2}$ | $9.29 \times 10^{-3}$ | $4.70 \times 10^{-3}$ | $2.68 \times 10^{-3}$ | 1.05 | 0.81 |
| $u$ | $1.20 \times 10^{-2}$ | $6.82 \times 10^{-3}$ | $3.60 \times 10^{-3}$ | $1.70 \times 10^{-3}$ | 1.93 | 0.94 |

Table 10: Shock-contact problem at $t = 0.25$: the top two rows give the contact location for the exact solution and the material-centered positions adjacent to the interface for the computed results on the finest grid (new method in the mixed cell, Tipton's method in the mixed cell, and the pure-material calculation), while the subsequent rows contain the corresponding flow field values for the various approaches.

| | Exact | New | Tipton | Pure |
| --- | --- | --- | --- | --- |
| $x_1$ | $5.72280 \times 10^{-1}$ | $5.72245 \times 10^{-1}$ | $5.72284 \times 10^{-1}$ | $5.72286 \times 10^{-1}$ |
| $x_2$ | | $5.72597 \times 10^{-1}$ | $5.72623 \times 10^{-1}$ | $5.72595 \times 10^{-1}$ |
| $p_1$ | 7.24981 | 7.24972 | 7.24978 | 7.24969 |
| $p_2$ | 7.24981 | 7.24972 | 7.24978 | 7.24969 |
| $\rho_1$ | 3.95809 | 3.97299 | 3.53063 | 3.78162 |
| $\rho_2$ | 2.57857 | 2.16434 | 2.36322 | 2.61504 |
| $e_1$ | 5.23327 | 5.21358 | 5.86685 | 5.47739 |
| $e_2$ | $7.02892 \times 10^{-1}$ | $8.37405 \times 10^{-1}$ | $7.66939 \times 10^{-1}$ | $6.93077 \times 10^{-1}$ |

for the new method and pure-material calculation bear greater similarity to each other than to Tipton's method, which exhibits a longer relaxation time and notably different time-dependence. Table 10 gives the values adjacent to the material interface at the final time on the finest grid, together with the exact solution at the contact interface. For both

Tipton and the pure-material calculation, the interface is slightly to the right (ahead) of where it should be; however, the new method gives slightly smaller (resp., larger) point-wise error for density and SIE in material 1 (resp., 2) than Tipton and the pure-material result. Fig. 25 shows the position of the material interface as a function of time. The results for all methods are similar, although, unlike the other problems, the pure-material interface (dashed line) and that of Tipton's method (dotted line) are slightly ahead of the interface of the new method (solid line).

## 5.5   Water-air shock tube

The water-air shock tube has become a standard test problem in the multi-material compressible flow community, as it tests inherently compressible flow features, uses a slightly more complicated and stiffer EOS than the standard polytropic gas, and possesses a directly computable solution. Variations of this problem have been evaluated by several researchers, including, e.g., Andrianov [1], Johnson & Colonius [16], Luo et al. [22], and Saurel & Abgrall [27].

The thermodynamic properties of water in this problem are given by the stiffened-gas EOS:

$$p = (\gamma - 1)\rho\varepsilon - \gamma p_\infty, \tag{5.6}$$

for which the square of the sound speed is given by

$$cs^2 = \gamma(\gamma - 1)\left(\varepsilon - \frac{p_\infty}{\rho}\right) = \gamma(p + p_\infty)/\rho. \tag{5.7}$$

The initial conditions for this problem, in mks units, are:

$$(\gamma, p_\infty, \rho, \varepsilon, p, u) = \begin{cases} \left(4.4, \, 6\times10^8, \, 10^3, \, 1.07\times10^6, \, 10^9, \, 0\right), & \text{if } 0 < x < 0.7, \\ \left(1.4, \, 0, \quad\quad 50, \quad 5\times10^4, \quad\quad 10^6, \, 0\right), & \text{if } 0.7 < x < 1, \end{cases} \tag{5.8}$$

with a final time of $t_{final} = 2.2\times10^{-4}$ s. The multi-material cell is initially centered at $x=0.7$ and contains the two materials specified above. The exact solution we use here is based on the solver described by Plohr [25].

Results of our method on this problem are shown in Figs. 26-30. Shown in Fig. 26 are, clockwise from the upper left, plots of the computed (solid line) and exact (dashed line) mass density, pressure, velocity, and SIE at the final time, together with the signed difference between these values (dashed lines), as well as the mixed-cell values (●). Notable are the undershoot in density and overshoot in SIE at the contact; the strong rarefaction is reasonably well captured. Fig. 27 shows results for all methods: the new method results are, again, closer to the pure-material calculation, while Tipton's method has greater under- and overshoots at the contact in mass density and SIE, respectively, together with a slight "bump" in pressure at the tail of the rarefaction. Table 11 gives the $L_1$ norm of the error between the computed results and the exact solution for these flow variables,

(a) Density



(b) Pressure
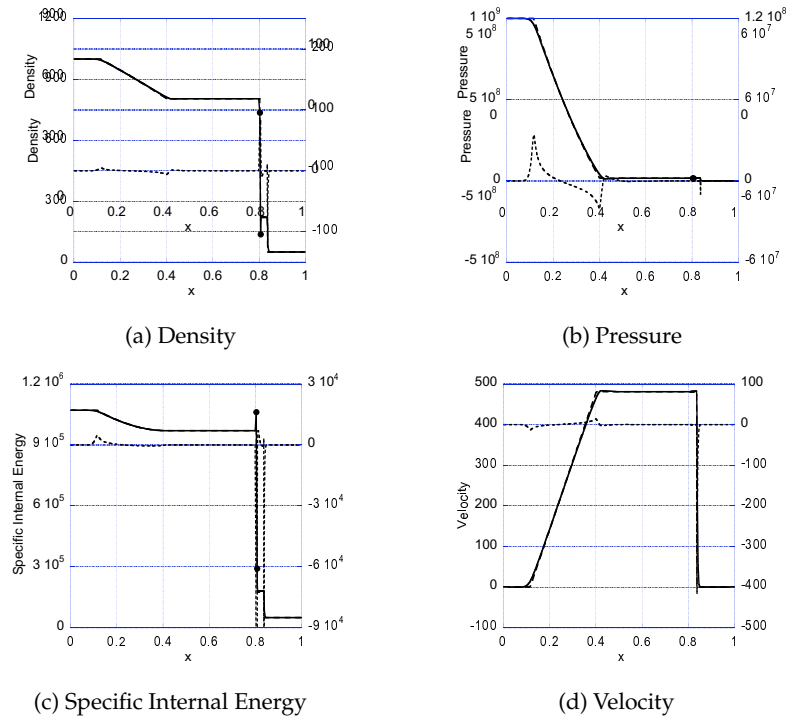


(c) Specific Internal Energy



(d) Velocity

Figure 26: Computed results (solid line) for the water-air shock tube problem with the new method for 249 zones on $[0,1]$ at $t = 2.2 \times 10^{-4}$. The difference (dotted line) between the computed and exact (dashed line) solutions is plotted against the right ordinate. The values corresponding to the individual materials in the mixed cell are denoted by the symbol ●.

for each of the three methods on all meshes, together with the fit of those results to the ansatz in Eq. (5.2). These values are depicted graphically in Fig. 28, showing that the magnitude of the errors for Tipton's method are notably greater than the other two approaches. Overall, these results imply first-order convergence of the methods for this problem.

Plots of time-histories for the three methods on the coarsest grid are shown in Fig. 29. The new method equilibrates monotonically in all quantities, while both Tipton's method and the pure-material calculation exhibit pressure undershoot (including negative pressure values) before equilibration. The new method and pure-material calculation are monotonic in material 2 (air), while the Tipton results are not. Also, the new method relaxes to final values that are closer to those of the pure-material calculation than to those of Tipton's method. Table 12 gives the values adjacent to the material interface at the final time on the finest grid, together with the exact solution at the contact interface. These point-wise values for the new method are closer to both the exact results and the pure-material calculations for all field quantities. Fig. 30 shows the position of the material interface as a function of time. In this case, the position of the material interface is very similar for all methods at all times.
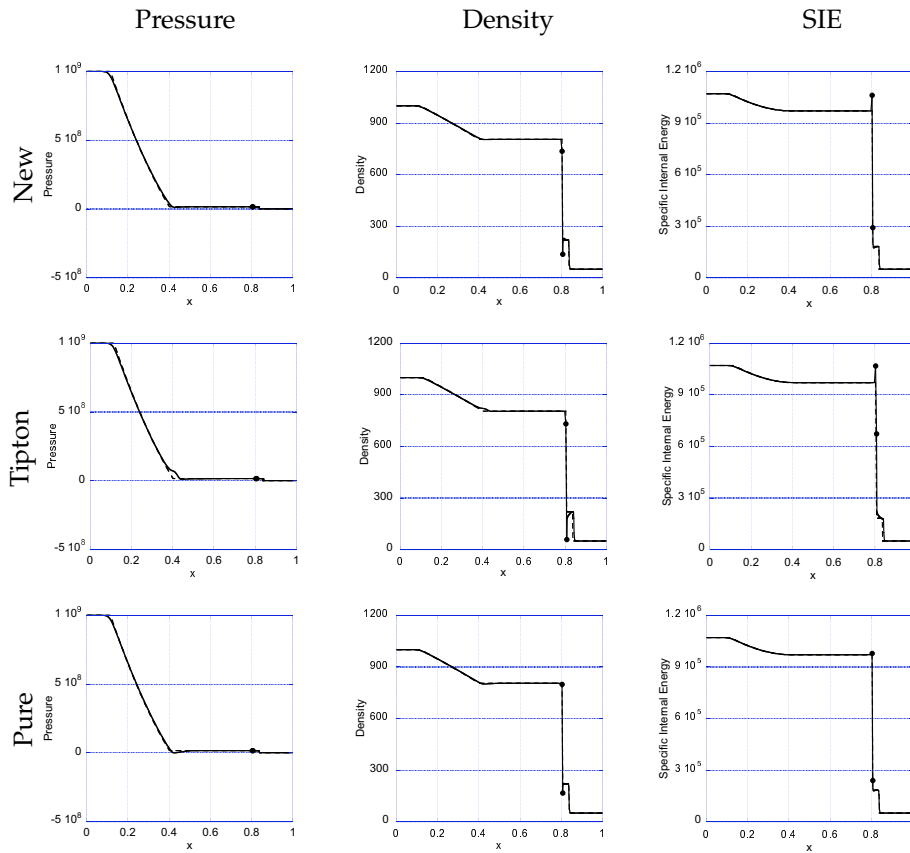
Figure 27: Results for the water-air shock tube problem on $[0,1]$ at $t=2.2\times10^{-4}$ for (from left to right) pressure, mass density, and SIE with (from top to bottom) the new method (249 zones), Tipton's method (249 zones), and the pure-cell calculation (250 zones). The computed results are the solid line and the exact solution is the dashed line.
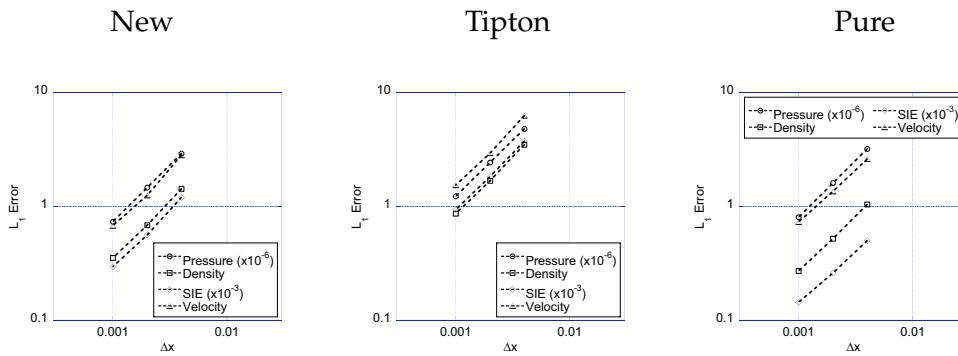


Figure 28: Plot of the $L_1$ norm of the difference between the computed results and exact solution on $[0,1]$ at $t=2.2\times10^{-4}$ for the water-air shock tube problem with the new method (left), Tipton's method (center) and the pure-material calculations (right). The values of the norm for the 249-, 499-, and 999-zone multi-material calculations and the 250-, 500-, and 1000-cell pure-material calculation are shown for the pressure ($\circ$), density ($\square$), SIE ($\diamond$), and velocity ($\triangle$). The curve fit parameters corresponding to these data are given in Table 11.
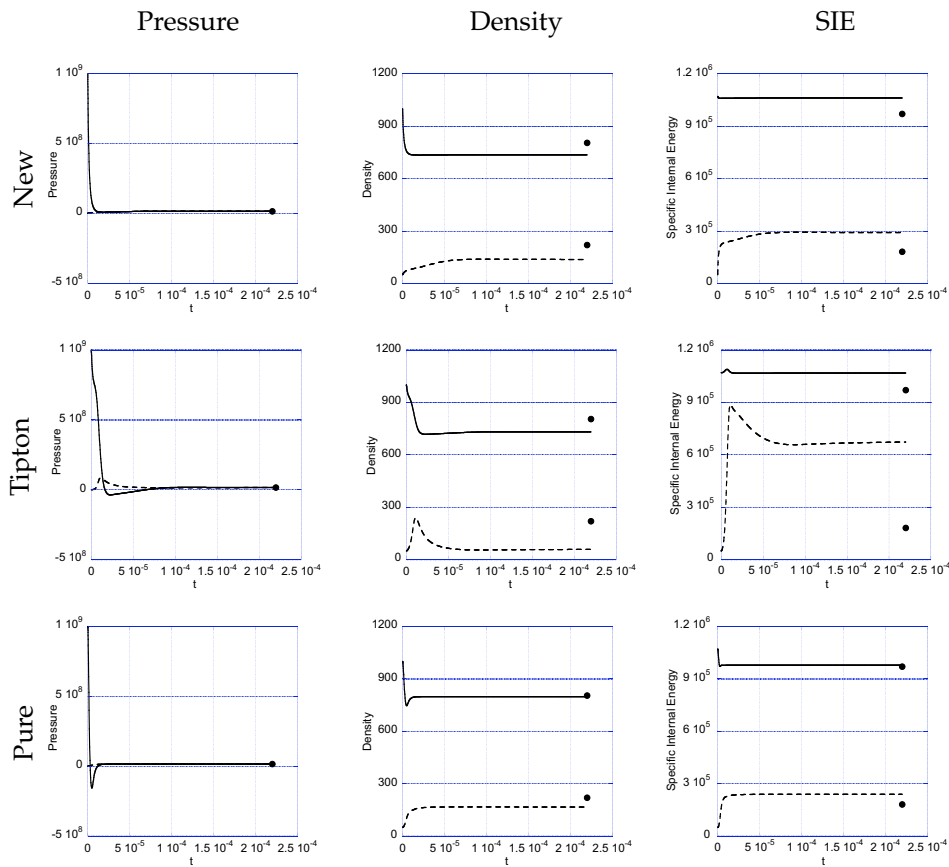
Figure 29: Time-history plots for the water-air shock tube problem on [0,1] for (from left to right) pressure, mass density, and SIE with (from top to bottom) the new method (249 zones), Tipton's method (249 zones), and the pure-cell calculation (250 zones). The solid line indicates the left material (material 1), the dotted line represents the right material (material 2), and the bullets represent the exact solution at the final time.
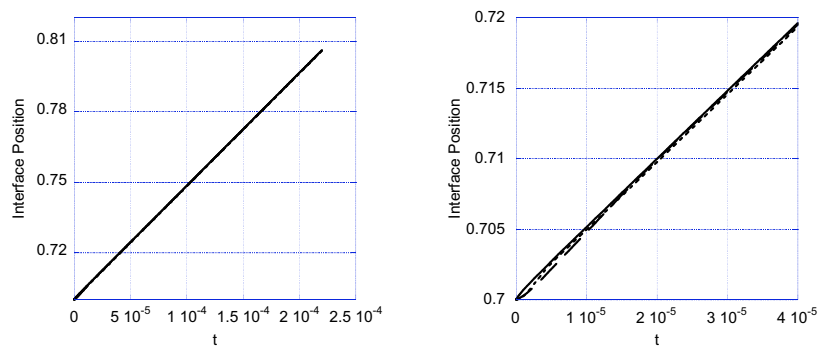


Figure 30: Plot of the position of the material interface as a function of time for the water-air shock tube problem on the coarsest mesh. The left plot shows the behavior for the entire simulation time, while the right plot shows the early-time behavior. The solid line corresponds to the new method, the dashed line to Tipton's method, and the dotted line to the pure-material calculation.

Table 11: $L_1$ norms of the difference between exact and computed water-air problem results, computed pointwise at $t = 2.2 \times 10^{-4}$, for the given variables with the indicated number of points on the unit interval for, from top to bottom, the new method, Tipton's method, and the pure-material calculation. The prefactor $\mathcal{A}$ and convergence rate $\sigma$ are least-squares fits to the relation given in Eq. (5.2). The values of $\sigma$ close to unity suggest first-order convergence.

| New Method | | | | | |
|---|---|---|---|---|---|
| | 249 | 499 | 999 | $\mathcal{A}$ $(\times 10^{-2})$ | $\sigma$ |
| $p$ $(\times 10^{-6})$ | 2.90 | 1.46 | $7.33 \times 10^{-1}$ | 6.95 | 0.99 |
| $\rho$ | 1.43 | 6.84 | $3.53 \times 10^{-1}$ | 3.63 | 1.01 |
| $e$ $(\times 10^{-3})$ | 1.20 | 5.62 | $2.96 \times 10^{-1}$ | 3.09 | 1.01 |
| $u$ | 2.81 | 1.25 | $6.75 \times 10^{-1}$ | 7.98 | 1.03 |

| Tipton's Method | | | | | |
|---|---|---|---|---|---|
| | 249 | 499 | 999 | $\mathcal{A}$ $(\times 10^{-2})$ | $\sigma$ |
| $p$ $(\times 10^{-6})$ | 4.77 | 2.42 | 1.23 | 10.7 | 0.98 |
| $\rho$ | 3.47 | 1.68 | $8.65 \times 10^{-1}$ | 8.67 | 1.00 |
| $e$ $(\times 10^{-3})$ | 3.72 | 1.83 | $9.31 \times 10^{-1}$ | 9.17 | 1.00 |
| $u$ | 6.23 | 2.93 | 1.53 | 16.4 | 1.01 |

| Pure Material | | | | | |
|---|---|---|---|---|---|
| | 250 | 500 | 1000 | $\mathcal{A}$ $(\times 10^{-2})$ | $\sigma$ |
| $p$ $(\times 10^{-6})$ | 3.18 | 1.60 | $8.03 \times 10^{-1}$ | 7.65 | 0.99 |
| $\rho$ | 1.04 | $5.21 \times 10^{-1}$ | $2.71 \times 10^{-1}$ | 2.18 | 0.97 |
| $e$ $(\times 10^{-3})$ | $5.00 \times 10^{-1}$ | $2.61 \times 10^{-1}$ | $1.44 \times 10^{-1}$ | 0.70 | 0.90 |
| $u$ | 2.60 | 1.35 | $7.29 \times 10^{-1}$ | 4.12 | 0.92 |

Table 12: Water-air shock tube problem at $t = 2.2 \times 10^{-4}$: the top two rows give the contact location for the exact solution and the material-centered positions adjacent to the interface for the computed results on the finest grid (new method in the mixed cell, Tipton's method in the mixed cell, and the pure-material calculation), while the subsequent rows contain the corresponding flow field values for the various approaches.

| | Exact | New | Tipton | Pure |
|---|---|---|---|---|
| $x_1$ | $8.05906 \times 10^{-1}$ | $8.05311 \times 10^{-1}$ | $8.05284 \times 10^{-1}$ | $8.05300 \times 10^{-1}$ |
| $x_2$ | | $8.06174 \times 10^{-1}$ | $8.06390 \times 10^{-1}$ | $8.06076 \times 10^{-1}$ |
| $p_1$ | $1.59868 \times 10^{7}$ | $1.59876 \times 10^{7}$ | $1.59817 \times 10^{7}$ | $1.59867 \times 10^{7}$ |
| $p_2$ | $1.59868 \times 10^{7}$ | $1.59876 \times 10^{7}$ | $1.59834 \times 10^{7}$ | $1.59867 \times 10^{7}$ |
| $\rho_1$ | $8.04979 \times 10^{2}$ | $7.35249 \times 10^{2}$ | $7.31464 \times 10^{2}$ | $7.98342 \times 10^{2}$ |
| $\rho_2$ | $2.20407 \times 10^{2}$ | $1.36417 \times 10^{2}$ | $5.90643 \times 10^{1}$ | $1.66948 \times 10^{2}$ |
| $e_1$ | $9.70426 \times 10^{5}$ | $1.06246 \times 10^{6}$ | $1.06796 \times 10^{6}$ | $9.78494 \times 10^{5}$ |
| $e_2$ | $1.81333 \times 10^{5}$ | $2.92991 \times 10^{5}$ | $6.76523 \times 10^{5}$ | $2.39395 \times 10^{5}$ |

# 6 Summary and conclusions

We have considered the problem of closing the system of equations for a two-material cell under the single velocity, single pressure assumption in one dimensional Lagrangian

hydrodynamics with mixed cells. We treat the constituents in these multi-material cells as distinct, which presents the problem of how to assign the thermodynamic states of the individual material components together with the nodal forces that such a zone generates, despite a lack of detailed information within such cells. Our approach is motivated by the work of Lagoutière [18] and Després & Lagoutière [10], in which the change in heat in the constituent materials in the mixed cell is assumed to be equal. Their mixed-cell model can be described by a set of four nonlinear equations in four unknowns consisting of the updated values of the specific internal energy and the specific volume for each of the two materials in the mixed cell. A solution to this set of nonlinear equations comprises one part of an overall predictor-corrector scheme for solving the governing conservation laws.

We break the assumption of instantaneous pressure equilibration among the mixed-cell constituents in the work of Lagoutière [18] and Després & Lagoutière [10] by imposing a sub-cell dynamics model that uses a minimization approach based on a local Riemann problem. The unique contribution of our work is the use of this physics-inspired, geometry-based approach both (i) to break instantaneous pressure equilibration by relaxing the individual sub-cell pressures to equilibrium and (ii) to determine the single updated value of the relaxing-toward-equilibrium pressure assigned to the overall mixed cell. We have provided the full equations for our method as well as a description of the algorithmic implementation.

We present results of our method for several test problems, each having a directly computable solution with either ideal-gas or stiffened-gas equations of state, together with complete details of the initial conditions for each problem. These results are compared with outcome of a pure-material (i.e., no mixed-cell) calculation (with two pure-material cells in place of the single multi-material cell) and with the results based on a standard implementation of Tipton's method [28, 30]. Quantitative evaluation of the difference between our computed results and the exact solutions demonstrates very nearly first-order convergence on each of these five problems. The mixed cell pressures in all problems evolve smoothly—but not necessarily monotonically—toward equilibrium on a timescale that decreases approximately linearly with mesh size. The mixed-cell solutions exhibit slight over- or undershoots in density (most noticeable in the shock-contact and water-air shocktube problems) and SIE (seen in the Sod, modified Sod, moving shock, and water-air shock tube problems). Comparison of these results with those using the Tipton's method or with those corresponding to a pure-material calculation indicate that the results of the new method are, overall, more similar to the pure-material calculations than to those using Tipton's method. While the overall $L_1$ norms of the errors are comparable on almost all problems, the challenging water-air shock tube problem exhibits a difference among the methods, with the new method having notably smaller $L_1$-error than the Tipton results and being qualitatively more similar to the pure-material calculation.

There remain other tests of these methods, e.g., on problems for which the material interface is not precisely in the center of the mixed cell; in particular, the case of a very

small initial volume fraction of one material poses a challenge for the class of methods we have considered. Further analysis of our approach, compared with and contrasted to a comparable analysis of Tipton's method, may provide valuable insights by which improved multi-material Lagrangian compressible flow algorithms can be developed.

## Acknowledgments

## References

[1] N. Andrianov, Analytical and numerical investigation of two-phase flows, Ph.D. dissertation, Universität Magdeburg (2003).

[2] M. Arora and P.L. Roe, On postshock oscillations due to shock capturing schemes in unsteady flows, J. Comput. Phys., 130 (1997), 25–40.

[3] J.W. Banks, D.W. Schwendeman, A.K. Kapila and W.D. Henshaw, A high-resolution Godunov method for compressible multi-material flow on overlapping grids, J. Comput. Phys., 223 (2007), 262–297.

[4] A. Barlow, A new Lagrangian scheme for multimaterial cells, in Proceedings of European Congress on Computational Methods in Applied Sciences and Engineering, ECCOMAS Computational Fluid Dynamics Conference, Swansea, Wales, U.K., 4–7 September 2001, 235–294.

[5] A.L. Bauer, D.E. Burton, E.J. Caramana, R. Loubère, M.J. Shashkov and P.P. Whalen, The internal consistency, stability, and accuracy of the discrete, compatible formulation of Lagrangian hydrodynamics, J. Comput. Phys., 218 (2006), 572–593.

[6] J. Campbell and M. Shashkov, A tensor artificial viscosity using a mimetic finite difference algorithm, J. Comput. Phys., 172 (2001), 739–765.

[7] E.J. Caramana, D.E. Burton, M.J. Shashkov and P.P. Whalen, The Construction of Compatible Hydrodynamics Algorithms Utilizing Conservation of Total Energy, J. Comput. Phys., 146 (1999), 227–262.

[8] P. Colella and H.M. Glaz, Efficient solution algorithm for the Riemann problem for real gases, J. Comput. Phys., 59 (1985), 264–289.

[9] V.I. Delov and V.V. Sadchikov, Comparison of several models for computation of thermodynamical parameters for heterogeneous Lagrangian cells, VANT (Mathematical Modeling of Physical Processes), 1 (2005), 57–70 (in Russian).

[10] B. Després and F. Lagoutière, Numerical resolution of a two-component compressible fluid model with interfaces, Prog. Comput. Fluid Dyn., 7 (2007), 295–310.

[11] E.A. Goncharov and Yu. Yanilkin, New method for computations of thermodynamical states of the materials in the mixed cells, VANT (Mathematical Modeling of Physical Processes), 3 (2004), 16–30 (in Russian).

[12] J.J. Gottlieb and C.P.T. Groth, Assessment of Riemann solvers for unsteady one-dimensional inviscid flows of perfect gases, J. Comput. Phys., 78 (1988), 437–458.

[13] C.W. Hirt, A.A. Amsden and J.L. Cook, An Arbitrary Lagrangian-Eulerian Computing Method for All Flow Speeds, J. Comput. Phys., 14 (1974), 227–253.

[14] X.Y. Hu, N.A. Adams and G. Iaccarino, On the HLLC Riemann solver for interface interactionin compressible multi-fluid flow, J. Comput. Phys. (2009), doi: 10.1016/j.jcp.2009.06.002.

[15] O.A. Hurricane and P.L. Miller, Shock Transmission and Reflection from a Material Interface and Subsequent Reflection from a Hard Boundary, Lawrence Livermore National Laboratory report UCRL-ID-132586 (1998) (unpublished).

[16] E. Johnson and T. Colonius, Implementation of WENO schemes in compressible multicomponent flow problems, J. Comput. Phys., 219 (2006), 715–732.

[17] J.R. Kamm and M.J. Shashkov, A Pressure Relaxation Closure Model for One-Dimensional, Two-Material Lagrangian Hydrodynamics Based on the Riemann Problem, Los Alamos National Laboratory report LA-UR-08-06045 (2008) (unpublished).

[18] F. Lagoutière, Modélisation Mathématique et Résolution Numérique de Problèmes de Fluides Compressibles à Plusieurs Constituants, Ph.D. dissertation, Université Pierre-et-Marie-Curie, Paris VI (2000) (in French).

[19] R. Landshoff, A Numerical Method for Treating Fluid Flow in the Presence of Shocks, Los Alamos Scientific Laboratory report LA-1930 (1955) (unpublished).

[20] R. LeVeque, Finite Volume Methods for Hyperbolic Problems, Cambridge University Press, Cambridge, UK (2002).

[21] R. Liska and B. Wendroff, Comparison of Several Difference Schemes on 1D and 2D Test Problems for the Euler Equations, SIAM J. Sci. Comput., 25 (2003), 995–1017.

[22] H. Luo, J. Baum and R. Löhner, On the computation of multi-material flows using ALE formulation, J. Comput. Phys., 194 (2004), 304–328.

[23] L.G. Margolin, Introduction to An Arbitrary Lagrangian-Eulerian Computing Method for All Flow Speeds, J. Comput. Phys., 135 (1997), 198–202.

[24] J. von Neumann and R. Richtmyer, A Method for the Numerical Calculation of Hydrodynamic Shocks, J. Appl. Phys., 21 (1950), 232–237.

[25] B. Plohr, Shockless acceleration of thin plates modeled by a tracked random choice method, AIAA J., 26 (1988), 470–478.

[26] L. Quartapelle, L. Castelletti, A. Guardone and G. Quaranta, Solution of the Riemann problem of classical gasdynamics, J. Comput. Phys., 190 (2003), 118–140.

[27] R. Saurel and R. Abgrall, A Multiphase Godunov Method for Compressible Multifluid and Multiphase Flows, J. Comput. Phys., 150 (1999), 425–467.

[28] M.J. Shashkov, Closure models for multimaterial cells in arbitrary Lagrangian-Eulerian hydrocodes, Int. J. Numer. Meth. Fluids, 56 (2007), 1497–1504.

[29] G. Sod, A Survey of Several Finite Difference Methods for Systems of Nonlinear Hyperbolic Conservation Laws, J. Comput. Phys., 27 (1978), 1–31.

[30] R.E. Tipton, CALE mixed zone pressure relaxation model, personal notes (1989) (unpublished).

[31] E. Toro, Riemann Solvers and Numerical Methods for Fluid Dynamics: A Practical Intro-

duction, Springer-Verlag, Heidelberg, Germany (1999).
[32] C.W. Wang, T.G. Liu, B.C. Khoo, A Real Ghost Fluid Method for the Simulation of Multi-medium Compressible Flow, SIAM J. Sci. Comput., 28 (2006), 278–302.
[33] C. Wang, H. Tang, T. Liu, An adaptive ghost fluid finite volume method fo rcompressible gas-water simulations, J. Comput. Phys., 227 (2008), 6385–6409.